Prediction and Predictability of High-Impact Western Pacific Landfalling Tropical Cyclone Vicente (2012) through Convection-Permitting Ensemble Assimilation of Doppler Radar Velocity

Lei Zhu,*,+,# Qilin Wan,# Xinyong Shen,+ Zhiyong Meng,* Fuqing Zhang,@
Yonghui Weng,@ Jason Sippel,&,** Yudong Gao,# Yunji Zhang,* and Jian Yue*

*Laboratory for Climate and Ocean–Atmosphere Studies, Department of Atmospheric and Oceanic Sciences,
School of Physics, Peking University, Beijing, China
+Key Laboratory of Meteorological Disaster of Ministry of Education, Nanjing University of Information
Science and Technology, Nanjing, China
#Key Laboratory of Regional Numerical Weather Prediction, Guangzhou Institute of Tropical and Marine
Meteorology, Guangzhou, China
@Department of Meteorology, The Pennsylvania State University, University Park, Pennsylvania
&I.M. Systems Group, Rockville, Maryland
**National Oceanic and Atmospheric Administration, Environmental Modeling Center, College Park, Maryland

ABSTRACT

The current study explores the use of an ensemble Kalman filter (EnKF) based on the Weather Research and Forecasting (WRF) Model to continuously assimilate high-resolution Doppler radar data during the peak-intensity stage of Tropical Cyclone (TC) Vicente (2012) before landfall. The WRF-EnKF analyses and forecasts along with the ensembles initialized from the EnKF analyses at different times were used to examine the subsequent evolution, three-dimensional (3D) structure, predictability, and dynamics of the storm. Vicente was an intense western North Pacific tropical cyclone that made landfall around 2000 UTC 23 July 2012 near the Pearl River Delta region of Guangdong Province, China, with a peak 10-m wind speed around 44 m s^{-1} along with considerable inland flooding after a rapid intensification process. With vortex- and dynamics-dependent background error covariance estimated by the short-term ensemble forecasts, it was found that the WRF-EnKF could efficiently assimilate the high temporal and spatial resolution 3D radar radial velocity to improve the depiction of the TC inner-core structure of Vicente, which in turn improved the forecasts of the track and intensity along with the associated heavy precipitation inland. The ensemble forecasts and sensitivity analyses were further used to explore the leading dynamics that controlled the prediction and predictability of track, intensity, and rainfall during and after its landfall. Results showed that TC Vicente's intensity and precipitation forecasts were largely dependent on the initial relationship between TC intensity and location and the initial steering flow.

1. Introduction

Landfalling tropical cyclones (TCs) are big threats to shipping and fishing interests far offshore and coastal and even inland areas. The accuracy of TC track, intensity, and associated rainfall forecasts near their landfall are of great importance for warning the public and protecting lives and property in the affected area. Over the last three decades, despite recent advances in TC track forecasts [Franklin (2004, updates available online at www.nhc.noaa.gov/verification); Cangialosi and Franklin (2011)], it remains difficult to predict intensity, structure, and precipitation amounts in TCs (Zou and Xiao 2000; Xiao et al. 2007; Houze et al. 2007; Rappaport et al. 2009; Cangialosi and Franklin 2011).

Besides the quality of forecast models, intensity prediction depends largely on how well the initial conditions can represent the inner-core structure that is strongly influenced by moist convection (Houze et al. 2007; Fovell et al. 2010). Landfalling TCs generally

Corresponding author address: Dr. Zhiyong Meng, Laboratory for Climate and Ocean–Atmosphere Studies, Department of Atmospheric and Oceanic Sciences, Peking University, School of Physics, 209 Chengfu Rd., Haidian District, Beijing 100871, China.
E-mail: zymeng@pku.edu.cn

spend most of their lifetime over the ocean, where the lack of sufficient conventional and high-resolution inner-core observations adds difficulty to the initialization of numerical weather prediction (NWP) models, which may be one of the most important factors in limiting the current operational forecast skill for TC intensity (Wang 2002; Hendricks et al. 2004; Montgomery et al. 2006; Rogers at al. 2006; Zhang et al. 2009, hereafter Z09).

Observations over the open sea that are capable of revealing the structure of TCs include satellite data, airborne and ground-based radar data, and aircraft reconnaissance data (including dropwindsonde data). Satellite data including both the radiance and satellite-derived atmospheric motion vector (AMV) observations do not contain detailed vertical structure information, and at present, cloudy or rainy radiances, especially over the TC inner-core regions, cannot be readily or efficiently ingested into NWP models to initialize TC vortices because of our current limited data assimilation capability (Liu et al. 2012; Xu et al. 2013). Doppler weather radar and aircraft reconnaissance data represent the only two currently available observations that can survey the TC inner core. Relative to aircraft data, Doppler weather radar data offers a more complete spatial and temporal coverage of precipitation and kinematic fields.

Studies have shown that assimilating ground-based radar radial velocity and reflectivity and airborne radial velocity through an ensemble Kalman filter (EnKF; Evensen 1994) can efficiently improve TC vortex initialization, structure, intensity, and precipitation in the Atlantic basin (Z09; Wu et al. 2010; Zhang et al. 2011; Xue and Dong 2013; Dong and Xue 2013; Weng and Zhang 2012, hereafter WZ12; Li et al. 2012; Aksoy et al. 2012, 2013; Sippel et al. 2013, 2014; Zhang and Weng 2015; Aberson et al. 2015). The EnKF uses an ensemble of short-term forecasts to estimate flow-dependent background error covariance and has been widely examined with various dynamical systems and adapted to realistic situations (Snyder and Zhang 2003; Zhang et al. 2004; Dowell et al. 2004; Tong and Xue 2005; Zhang et al. 2006; Fujita et al. 2007; Meng and Zhang 2007, 2008a,b; Aksoy et al. 2009, 2010; Zhang et al. 2011; WZ12; Zhang and Weng 2015).

Tropical cyclones are frequent in the western North Pacific (WNP), and landfalls along China's coast commonly cause severe damage. In WNP, there are no operational airborne Doppler radar observations, and only ground-based radar observations are available. The Chinese ground-based Doppler radar network is now in its final development stage after a decade of deployment, expansion, and calibration. The averaged distance between two neighboring Doppler weather radars in eastern China is about 180 km near the coast, which is smaller than that in the eastern United States (about 228 km according to our rough calculation). Though these radars have similar technology and data formats to those of the WSR-88Ds in the United States, their potential contribution to analyses and forecasts of landfalling TCs has not been fully examined. Though Wang et al. (2014) examined the impact of assimilating Taiwan ground-based radar data at the peak stage of landfalling TC Jiangmi using an ARPS-based EnKF system, the improvement in the analysis and forecast with the EnKF assimilation of radar data was rather limited. Effective assimilation of coastal ground-based radar data is an important reference point for the potential development of an operational modeling system for WNP TC forecasting, which would be beneficial for TC-associated disaster prevention and mitigation.

In July 2012, TC Vicente made landfall in Guangdong China at 2000 UTC 23 July 2012 near the Pearl River Delta region (Figs. 1a,b), one of the most populated and industrialized areas in China. It caused severe flooding and 15 fatalities in the affected area. The direct economic loss was about $329 million (U.S. dollars). Vicente was one of the strongest landfalling storms to ever hit the Pearl River Delta. It formed at 1200 UTC 18 July 2012 to the east of Luzon Island. Vicente moved generally west-northwest in a trochoidal pattern (Fig. 1b) and rapidly intensified on 23 July (Figs. 1c and 2a). The maximum surface wind speed (maxWSP) increased from $25.7 \, \mathrm{m \, s^{-1}}$ at 1800 UTC 22 July to $43.7 \, \mathrm{m \, s^{-1}}$ at 1800 UTC 23 July according to the best track estimate of Hong Kong Observatory (HKO) (Fig. 1c), thus satisfying the criteria of rapid intensification for the WNP TCs [$15.4 \, \mathrm{m \, s^{-1}}$ or 30 kt in 24 h by Wang and Zhou (2008)]. There was quite a large uncertainty in the intensity estimate of Vicente from different monitoring agencies (Figs. 1c and 2a); we chose to use HKO (with a 10-min sampling period) best track data since it was roughly in the middle of all the available best track estimates. This large uncertainty was likely related to different sampling periods in wind definitions, the lack of sufficient direct observations, and inconsistencies in the use of the Dvorak technique by different centers.

This work examines the impact of assimilating Guangzhou radar data when Vicente started to enter the radar coverage (radar location and velocity coverage is given in Fig. 1b) throughout the period of its highest intensity and remained within radar coverage for 18 h. The official TC intensity forecast and operational guidance during Vicente's rapid intensification were all too weak (Shieh et al. 2013), which partly motivated this data assimilation study.

The purpose of this work is twofold: 1) to show the potential benefit of assimilating coastal Chinese radar
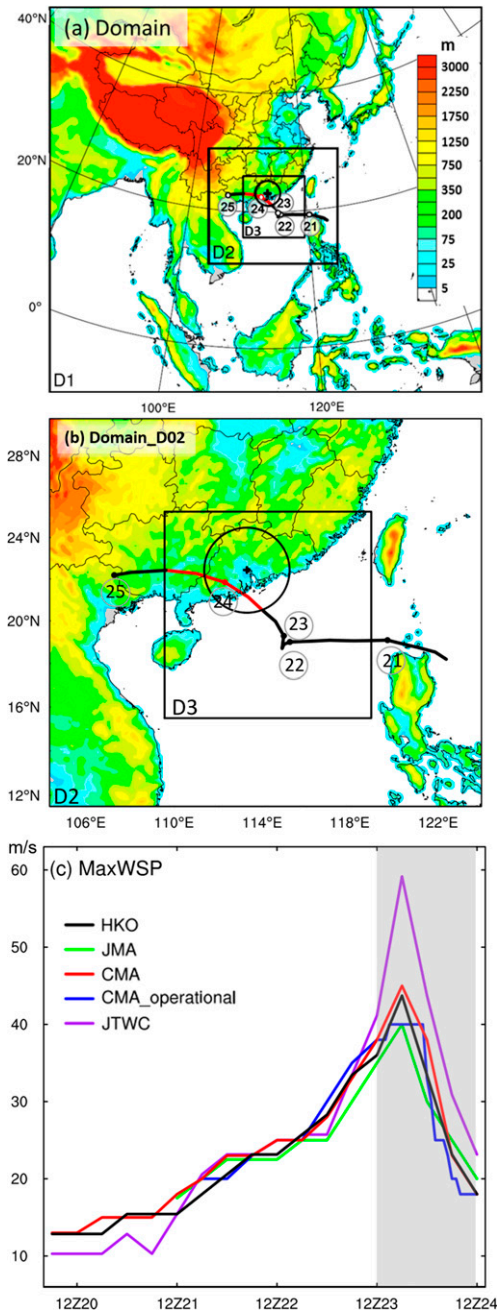
FIG. 1. (a) Model domain configuration. Also shown is the HKO best track (black line) of Vicente (2012) starting from 0600 UTC 20 Jul to 0000 UTC 25 Jul 2012. The red part denotes the period between 1200 UTC 23 Jul and 1200 UTC 24 Jul during which the numerical experiments were performed. All the positions at 0000 UTC were marked by a white dot with the date given in the white circle. Also given is the location (black cross mark) and radial velocity coverage (black circle) of Guangzhou Doppler radar and the terrain elevations (color shaded, m MSL). (b) A close-up of the area within D2. (c) The maximum surface wind speed (maxWSP) from the best track estimates of TC Vicente of the Hong Kong Observatory (HKO), the Japan Meteorological Agency (JMA), the China Meteorological Administration (CMA, final estimate after TC season), CMA_operational (real-time estimate), and the Joint Typhoon Warning Center (JTWC). The data assimilation period is shaded in gray.

data with an EnKF analyses in the WNP high-impact, landfalling TC Vicente; and 2) to examine the prediction and predictability of the track, intensity, and rainfall of Vicente based on the EnKF analysis and forecasts. In particular, the forecast uncertainty of the minimum SLP, the storm-associated rainfall, and key controlling factors of the forecast uncertainties were examined through ensemble sensitivity analyses based on ensemble forecasts initiated with the EnKF analyses and perturbations.

Section 2 introduces the numerical modeling system, the EnKF technique, the processing of the observations to be assimilated, and the experiment setup. Section 3 presents EnKF analyses of Vicente in terms of track, minimum SLP, and the TC 3D structure. Section 4 shows the comparison among observations, experiments without data assimilation, and forecasts initialized with EnKF analyses. The results of sensitivity analyses using the ensemble forecasts are given in section 5. The last section gives the summary and some discussion.

2. Methodology

a. WRF and EnKF

The numerical model used in this work was the Advanced Research version of the Weather Research and Forecasting (WRF) Model (ARW) version 3.3 (Skamarock et al. 2008). Three two-way nested domains were used with 35 vertical levels, a model top at 10 hPa, 202×181, 181×163, and 259×259 grid points in the horizontal, and grid spacings of 40.5, 13.5, and 4.5 km for D1, D2, and D3, respectively (Fig. 1a). The initial and boundary conditions were provided by the $1° \times 1°$ and 6-hourly final analyses (FNL) of the Global Forecast System from the National Centers for Environmental Prediction (NCEP; NOAA/National Centers for Environmental Prediction 2000). The Grell–Devenyi cumulus scheme (Grell and Devenyi 2002) for the outermost domain (D1), the WRF single-moment (WSM) 6-class microphysics scheme with graupel (Hong et al. 2004), and the Yonsei State University (YSU) scheme (Noh et al. 2003) for planetary boundary layer (PBL) processes were used in this work.

The WRF-based EnKF system used in this work is the same as in Z09 and WZ12, which was originally developed for regional-scale data assimilation in Meng and Zhang (2008a,b). The ensemble size was 60. The initial ensemble members were generated by adding perturbations, which were randomly sampled from the default "cv3" background error covariance option in the WRF 3DVar package [refer to Barker et al. (2004) for details], to the FNL/NCEP analysis data at 0000 UTC 23 July 2012. The perturbed variables included horizontal wind components (u, v), potential
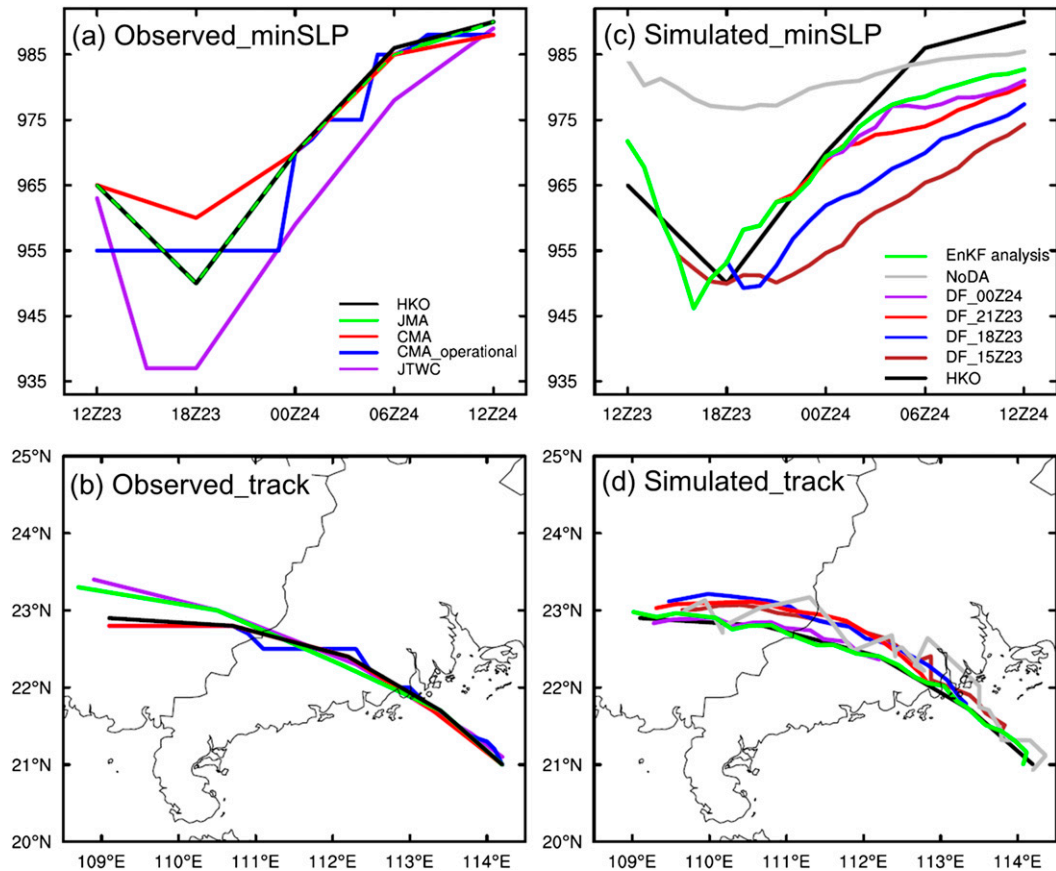
FIG. 2. (a),(b) The best track estimate of TC Vicente from HKO, JMA, CMA, CMA_operational, and JTWC, as well as (c) the simulated intensity in terms of minSLP (hPa) and (d) the positions of Vicente in the deterministic WRF forecasts (color curves) initialized with the EnKF analyses every 3 h from 1500 UTC 23 Jul to 0000 UTC 24 Jul 2012 in comparison with the best track estimate from HKO.

temperature and mixing ratio for water vapor, and the standard deviations of $2\,m\,s^{-1}$ for wind, $1\,K$ for temperature, and $0.5\,g\,kg^{-1}$ for mixing ratio [similar perturbations have been used by Meng and Zhang (2008a,b), and Z09] approximated by the analysis error of the FNL data (surface error of NCEP FNL is available online at http://polar.ncep. noaa.gov/mmab/papers/tn233/mmab233.pdf). Similar perturbations were also used to represent the boundary condition uncertainties of the ensemble. The covariance relaxation method proposed by Zhang et al. [2004, their Eq. (5)] was used to inflate the background error covariance with a relaxation coefficient of 0.8 (Z09; WZ12). Data assimilation was performed for all domains. The prognostic variables of perturbation potential temperature (T), vertical velocity (W), horizontal wind components (U and V), mixing ratio for water vapor (QVAPOR), cloud water (QCLOUD), rainwater (QRAIN), perturbation geopotential (PH), perturbation dry air mass in column (MU), surface pressure (PSFC), and perturbation pressure (P) were updated. The successive covariance localization

(SCL) method (proposed by Z09) was used with the horizontal localization radius of influence (ROI) of 1215, 405, and 135 km for D1, D2, and D3, respectively, using the fifth-order correlation function proposed by Gaspari and Cohn (1999). The ROI in the vertical direction was set to the model depth. This approach has been adopted in several previous papers (e.g., Z09; WZ12; Zhang and Weng 2015).

b. Guangzhou Doppler radar data processing and superobservations

The radial velocity data from the Guangzhou radar located in the south China coast (Fig. 1b) were assimilated by the EnKF. This is an S-band Doppler radar that is similar to the WSR-88Ds of the United States (Zhu and Zhu 2004). Given that the Chinese Doppler radar network is still in the development stage, and there is no uniform software to process the radar observations, a considerable amount of our initial effort was invested to decode and quality control the data. We first converted
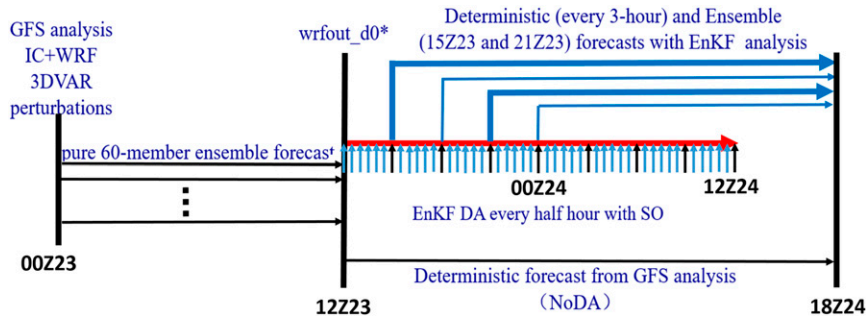
FIG. 3. The schematic flowchart for the EnKF and NoDA experiments. The small vertical arrows together with the heavy red arrow between 1200 UTC 23 Jul and 1200 UTC 24 Jul represent EnKF cycling at half-hour intervals. The thin black arrow between 1200 UTC 23 Jul and 1800 UTC 24 Jul represents the deterministic forecast initiated from the GFS analyses (NoDA). The thin and heavy blue arrows denote deterministic and ensemble forecasts initiated during 1500 and 2100 UTC 23 Jul.

the full-3D-volume radial velocity data to the format equivalent to that of Level-II data from WSR-88D. The NCAR radar editing software (SOLO-II) (Oye et al. 1995) was then used to do velocity unfolding manually. We further used the superobservation (SO) procedure developed by Z09 to combine multiple observations with additional quality control. The observation error for radial velocity was $3\,m\,s^{-1}$.

c. Experimental design

As shown in the schematics of Fig. 3, the ensemble was first integrated for 12 h to develop a high-resolution, flow-dependent background error covariance structure. Starting at 1200 UTC 23 July, SOs were assimilated every half hour until 1200 UTC 24 July, during which TC Vicente experienced a rapid intensification and peak intensity followed by landfall (shaded in Figs. 1c and 2a). Deterministic forecasts were initiated from the ensemble mean of the EnKF analyses every 3 h starting from 1500 UTC 23 July to 0000 UTC 24 July. Two ensemble forecasts were performed starting from 1500 and 2100 UTC 23 July, respectively. As a benchmark, "NoDA" was performed as a deterministic forecast initiated from the NCEP FNL analyses at 1200 UTC 23 July without data assimilation. All these forecast experiments were integrated to 1800 UTC 24 July by which time the observed storm had nearly completely dissipated.

3. The EnKF analyses

a. Track and minimum SLP

The analyzed minimum SLP (referred to as minSLP hereafter as a proxy for TC intensity) and position of Vicente from the continuous EnKF analysis are shown in Figs. 2c and 2d (green line). Considering the possible intensity forecast bias in comparing the instantaneous

raw model results to the HKO best track data in terms of maximum surface wind velocity, which is an average over a certain sampling period, we chose to discuss the TC intensity only in terms of minSLP hereafter. A 10-min sampling period is used by HKO to estimate surface wind. Besides, there is usually large uncertainty in wind estimate even with a same sampling period. For example, Landsea and Franklin (2013) found that the uncertainties of the best track estimates in the Atlantic basin have an error bar of over $5\,m\,s^{-1}$ for maximum 10-m winds and over 6 hPa for minSLP.

The EnKF analyses successfully captured the evolution of Vicente in terms of both minSLP and track (Figs. 2c,d). The impact of the radar data assimilation can be best seen through direct comparison with "NoDA" directly initialized from the FNL analysis without ingesting any additional observations throughout the model integration. The most noticeable effect of Doppler radar assimilation was upon the minSLP estimate in Fig. 2c (EnKF analyses, green; NoDA, gray). In particular, the EnKF analysis was able to decrease the minSLP toward the best track minSLP within 2–3 h after assimilating only 3–4 volumetric Doppler velocity observations. Except for a negative bias at 1600 UTC 23 July and after 0300 UTC 24 July, the EnKF estimates of the minSLP matched closely with the HKO best track estimate. This benefit can be clearly seen in the evolution and mean (Fig. 4a) of the absolute minSLP error during the 12 h around the minimum minSLP point. The mean absolute minSLP error decreased by about 17 hPa.

With the continuous assimilation of the Doppler radar data, the track in the EnKF analysis (green line, Fig. 2d) followed the best track estimates well, including the meandering segment after landfall. In contrast, the track of NoDA had a marginally rightward bias relative to
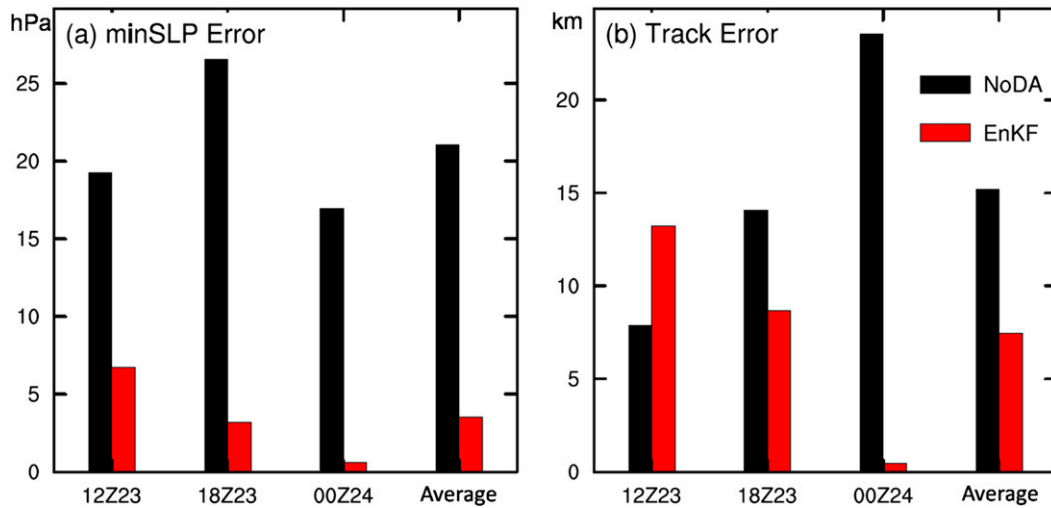
FIG. 4. The TC (a) minSLP and (b) track error around TC landfall for the EnKF analyses and NoDA experiments at different times as well as an average over the three times.

the best track and a large variability from hour to hour. This noise was also reflected in the track error evolution during the 12 h around the minimum minSLP point (Fig. 4b). NoDA had a smaller error at 1200 UTC than that of the EnKF and then a consistent larger error after 1800 UTC. However, the EnKF analysis track still showed a decrease of the mean error of about 8 km (Fig. 4b).

b. TC 3D structure

Moving beyond point metrics of track and minSLP, Fig. 5 shows the EnKF analyses of the 0.5° base scans of the radial velocity at selected times verifying with independent unassimilated observations from the Guangzhou radar, which were randomly chosen from the total SOs (~10% of total SOs), in comparison with the "NoDA" simulation without Vr assimilation. Promisingly, even after the first volumetric Vr assimilation cycle at 1200 UTC 23 July, the EnKF analysis (Fig. 5b) was able to capture well the observed radial velocity dipole pattern (Fig. 5a). At this time, the root-mean-squared error (RMSE) of radial velocity for the EnKF analysis (red in Fig. 6) was about 2 m s^{-1} smaller than that of NoDA (gray in Figs. 6 and 5c), mainly due to a more accurate representation of TC structure and minSLP (Figs. 4a and 5b). Except for those very small-scale features or over complex terrain, the EnKF estimate of the 0.5° base scan further improved over time with respect to verifying independent observations, while the NoDA estimates deviated farther and farther from the observations (Figs. 5d–l and 6). The largest improvement (about 4 m s^{-1}) was observed at the minimum minSLP stage of 1800 and 2100 UTC 23 July (Fig. 6).

The evolution of observation-based statistics during the EnKF cycling was then examined in terms of the RMSE of radial velocity (Fig. 7a). The error growth rate was larger during the first 6 h before the TC reached its minimum minSLP with a peak error growth rate near the TC minimum minSLP. The error growth rate decreased slightly in the next 6 h when the TC started to weaken. The error of radial velocity saturated starting at about 0300 UTC 24 July, which was about 15 h into the EnKF cycling. The impact of observations on the prior became quite small thereafter. The small impact from the observation in later stages can also be clearly seen in either the evolution of the TC minSLP and track at 30-min intervals from prior to posterior estimations even early from 2100 UTC 23 July (Figs. 7b,c) or the errors of prior and posterior at the 6-h interval (Figs. 7d,e). Though the error improvement became smaller in the later cycles ("convergence or saturation"), the observations were still likely responsible for maintaining the level of convergence.

To further explore the impact of assimilating Doppler velocity observations, Fig. 8 shows the EnKF analysis increments of 850-hPa horizontal wind vectors and potential temperature. Consistent with the improvement seen in Fig. 5, the EnKF analysis after the first cycle of radar data assimilation produced a clear asymmetric cyclonic pattern around the observed center of Vicente (Fig. 8a) with the largest increments appearing to the northeast. This asymmetric cyclonic increment of the wind resulted in a stronger circulation (Fig. 2c). Correspondingly, there was an overall increase (decrease) of potential temperature inside (just outside) the inner core, as more clearly seen from a direct comparison of
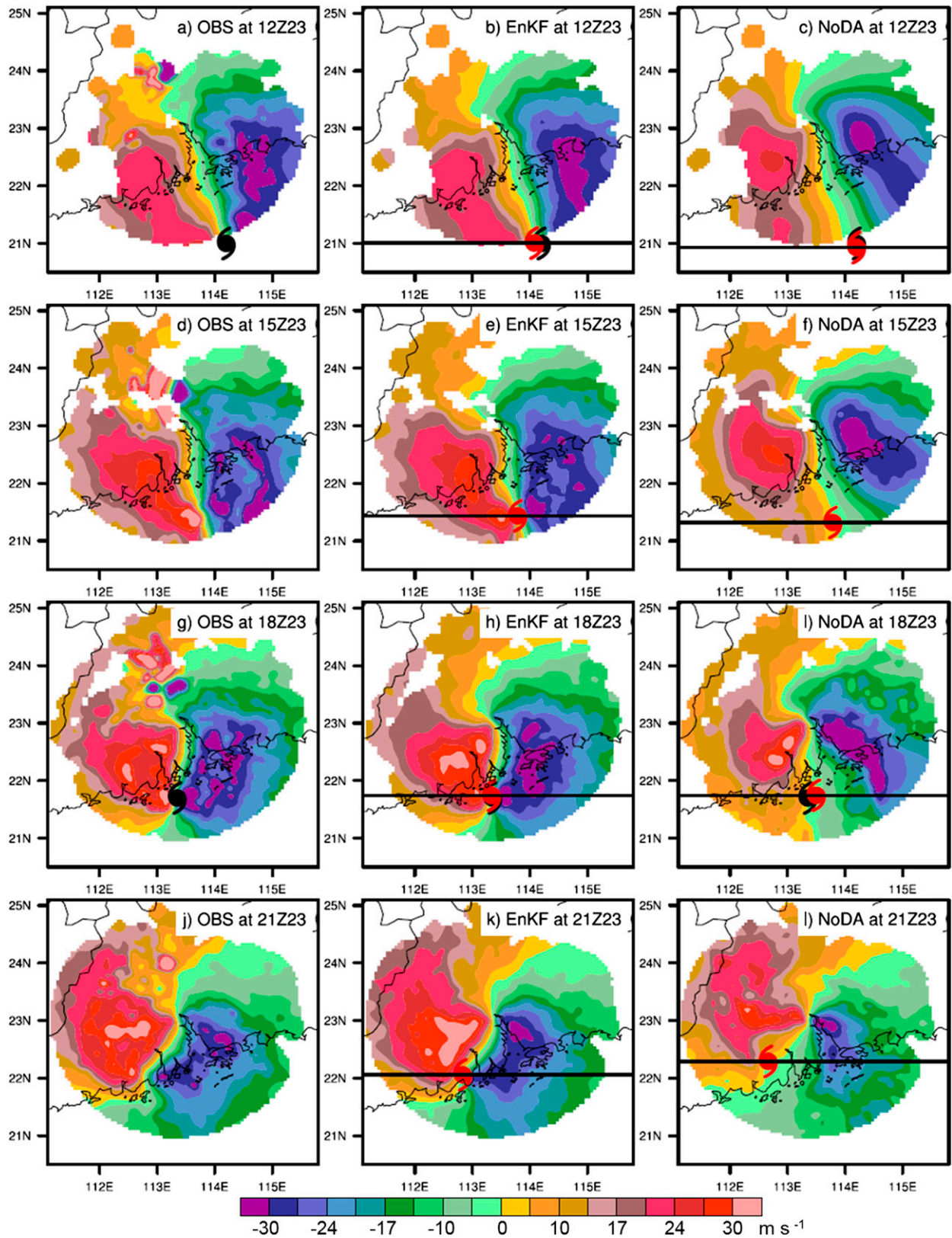
FIG. 5. (a),(d),(g),(j) The raw radial velocity (m s^{-1}) observations from the 0.5° base scan of the Guangzhou radar (OBS); (b),(e),(h),(k) the corresponding EnKF analyses; and (c),(f),(i),(l) the NoDA forecast valid at 1200, 1500, 1800, and 2100 UTC 23 Jul 2012, respectively. The TC mark denotes the corresponding TC center (red for the simulated and black for the observed).
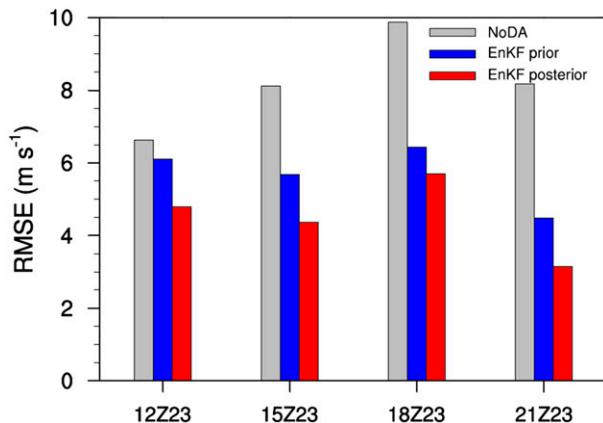
FIG. 6. The RMSE of radial velocity of the prior forecasts and posterior analyses of the EnKF in comparison with the RMSE of NoDA forecasts at different times.

horizontal wind speed and potential temperature between the EnKF and NoDA in the vertical cross sections through the simulated TC center (Figs. 9a vs 9e). The EnKF-analyzed TC had a smaller radius of maximum winds and a deeper warm core. A stronger thermal gradient in the eyewall region is consistent with stronger tangential winds, suggesting that the ensemble-based covariance estimate is congruent with the underlying TC dynamics. Also at the first analysis time, there were broad areas of considerable wind and temperature increments over land away from the TC center (Fig. 8a) as well as over the open ocean (not shown). The ensemble sensitivity analysis (to be discussed in section 5) suggests that these analysis increments may be critical in leading to a better track and minSLP forecast during and after landfall.

As more volumes of Doppler data were assimilated, and the priors of subsequent analysis cycles became more accurate (Fig. 6), the analysis increments became more focused near the vortex core and vicinity (Fig. 8). Though not shown explicitly, the more focused and stronger TC vortex in the EnKF analysis was again evident in the cross sections of Fig. 9 in comparison to NoDA.

At 2100 UTC 23 July, just after the landfall (Fig. 8d), both the temperature and wind increments were greatly reduced in areal coverage and magnitude compared to the initial analysis time (Fig. 8a) at different levels. The TC vortex also underwent dramatic adjustment, especially in the wind field, right before and after the landfall as seen in the EnKF analyses in Figs. 9g and 9h. The boundary layer wind to the east of the vortex center greatly reduced in magnitude due to strong interaction with land (and friction) though this effect was smaller in NoDA (Figs. 9c,d).

It is also worth noting that there were only small and sporadic analysis increments in the outer region of TC at the later analysis times (Figs. 8c,d). This was also a reflection of the tropical storm dynamics: the larger-scale features in the outer part of the TC had likely already been adequately adjusted by earlier observations (and there was no apparent growth of large-scale error), thus requiring less frequent and less dense observations.

The impact of assimilating Doppler radar in the wind field was clearly seen in the radius–time evolution of the azimuthally averaged tangential winds at 850 hPa (Fig. 10). Although NoDA captured some strengthening of the mean vortex shortly before landfall (2000 UTC 23 July), the maximum mean 850-hPa tangential wind with the EnKF radar analysis was at least $10\,\mathrm{m\,s^{-1}}$ larger than that of NoDA for most of the duration before and after landfall. Moreover, the radius of maximum tangential wind in the EnKF analysis was about half of that in NoDA, indicating a much stronger and more compact storm of Vicente.

4. Deterministic forecast initiated with the EnKF analysis

a. Track and minSLP

As also shown in Figs. 2c and 2d, progressively better track and minSLP predictions were obtained in consecutive deterministic forecasts initiated every 3 h from the EnKF analyses after more and more 3D volumetric radar data were assimilated (in comparison to NoDA verifying against HKO best track estimates). With more Doppler radial velocity data assimilated, the simulated tracks also became less noisy compared to that in NoDA. Slightly northward bias were observed in the deterministic forecasts initiated at 1500, 1800, and 2100 UTC 23 July, while a much smaller track error was observed in the deterministic forecast initiated at 0000 UTC 24 July. The forecast landfall locations and times initialized from both the 1500 and 1800 UTC EnKF mean analyses matched well with the observations (Fig. 2d). All the deterministic forecasts initiated from the EnKF analyses showed clear improvement in the minSLP simulation compared with NoDA in terms of minSLP before landfall. Despite some timing error, likely due to the random nature of individual intense convective cells, forecasts from both the 1500 and 1800 UTC runs also captured the observed minimum minSLP very well. However, for the reasons not completely clear, both the 1500 and 1800 UTC forecasts failed to weaken the TC as fast as in the observations right after landfall (Fig. 2c). This was less evident in the continuous EnKF analysis (green) or in forecasts
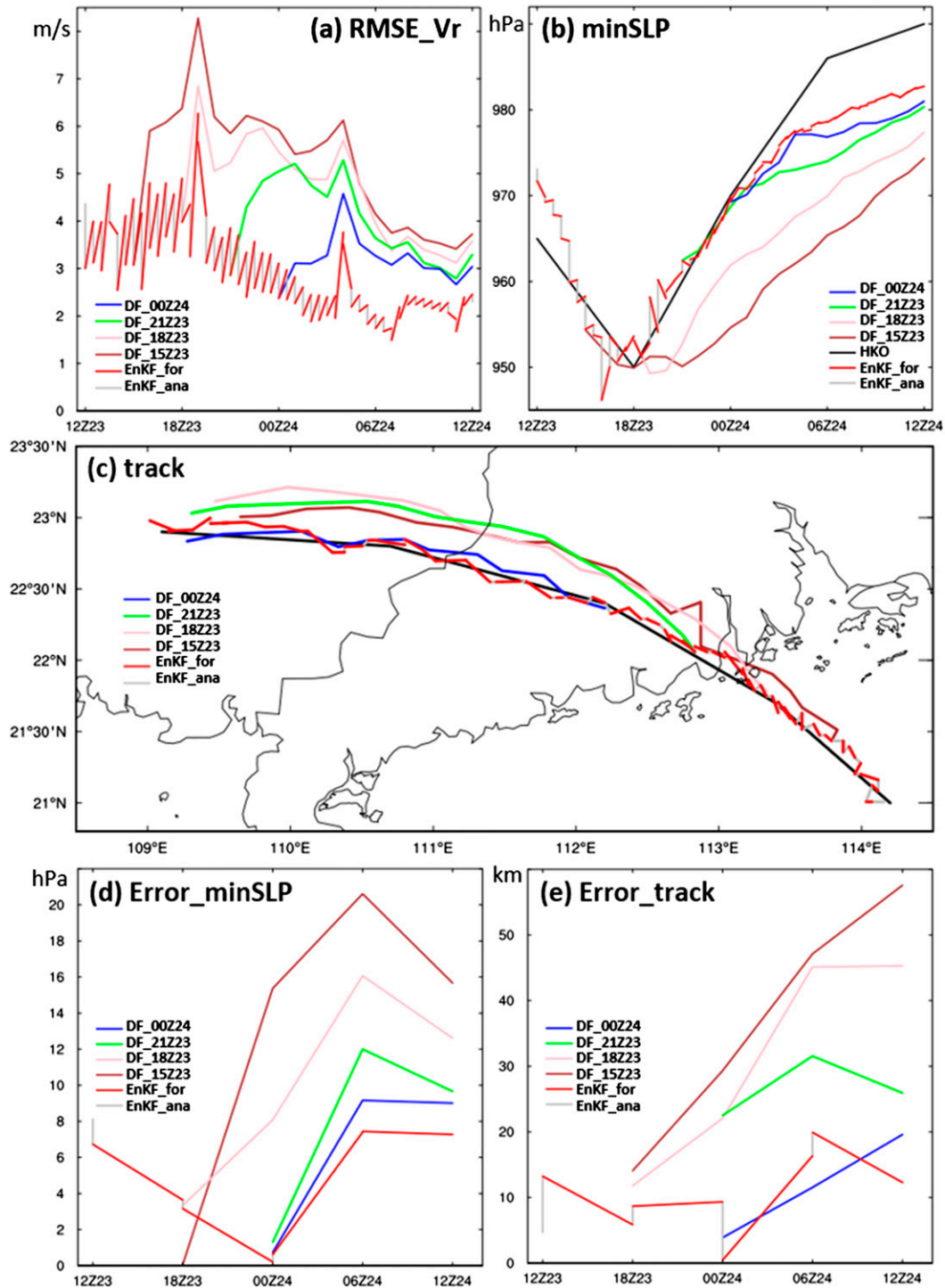
FIG. 7. The evolution of the RMSE of (a) radial velocity, (b) minSLP, (c) track, (d) error_minSLP, and (e) error_track in EnKF and deterministic forecast experiments. EnKF_for and EnKF_ana represent the forecast and analysis stage of the EnKF cycles, respectively.

initialized after landfall. Similar results were also observed in Du et al. (2012) and Dong and Xue (2013).

The relative performance among different deterministic forecasts can be seen more clearly in terms of their actual errors (Figs. 7a,d,e). Longer time data assimilation produced progressively smaller forecast errors of minSLP, track, and also radial velocity likely due to the improved TC positions. In all the deterministic forecast
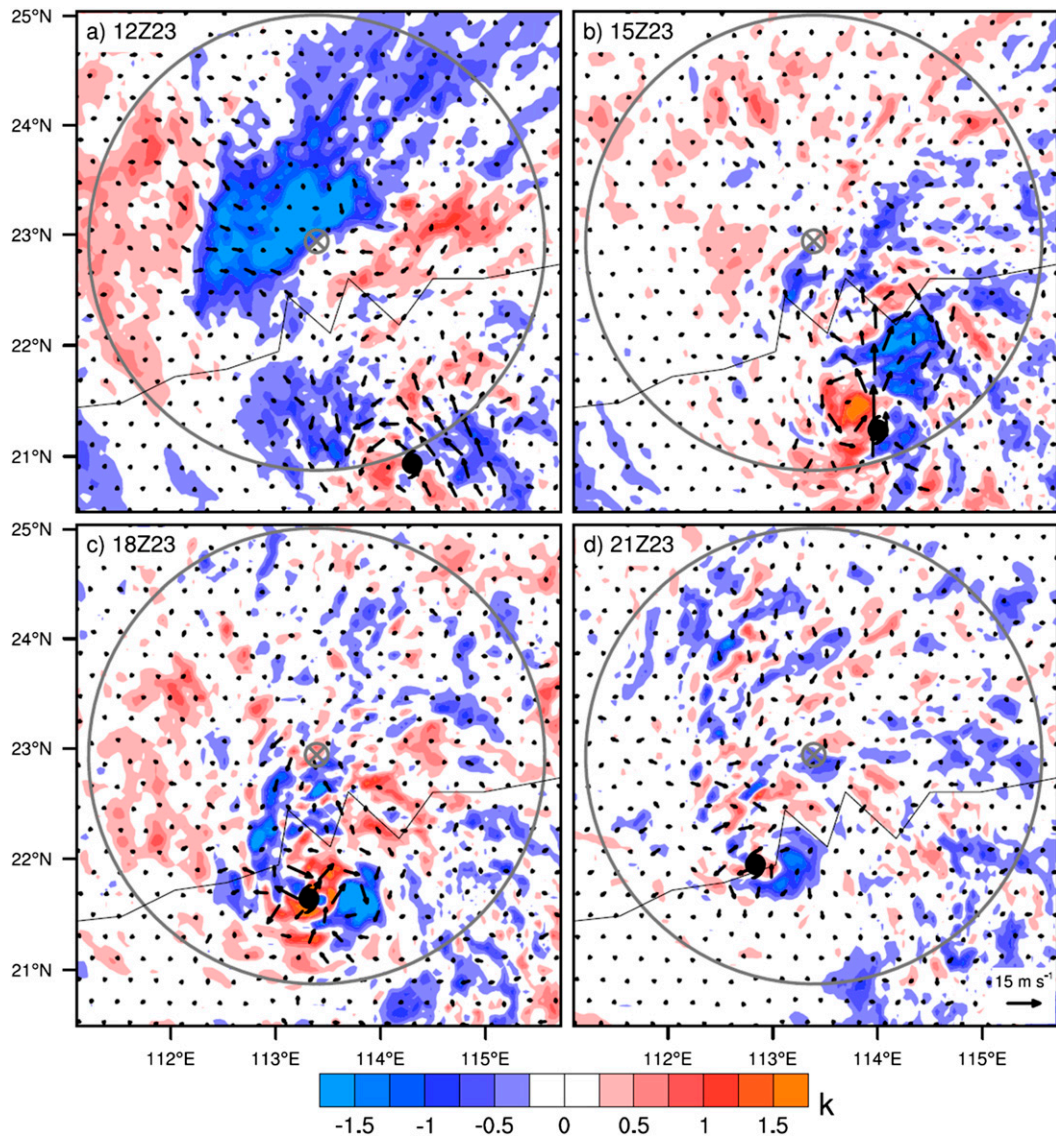
FIG. 8. The EnKF-analysis increments of 850-hPa potential temperature (shaded, K) and wind (vector, m s^{-1}) valid at (a) 1200, (b) 1500, (c) 1800, and (d) 2100 UTC 23 Jul 2012. The black dot denotes the HKO best track estimate of the TC center position. The gray circle denotes Vr coverage of the Guangzhou radar.

experiments, the RMSE of radial velocity rapidly increased during the first three hours then decreased gradually with similar oscillations. The largest errors were all observed near the minimum minSLP point.

Generally speaking, the deterministic forecasts initiated from the EnKF analyses with radar data assimilation produced better track and minSLP simulations for Vicente relative to NoDA. These results clearly demonstrate the significance and potential of assimilating land-based Doppler radar observations with an EnKF in the initialization and prediction for intense coastal storms such as Vicente. This complements an earlier study of Z09 that assimilated WSR-88D ground-based

Doppler velocity observations to simulate the formation stages of a TC over the Gulf of Mexico [Hurricane Humberto (2007)].

b. Precipitation and hazards

In addition to TC track and minSLP, the EnKF radar data assimilation also improved the forecasts of 1-h accumulated rainfall. Figure 11 compares the 1-h rainfall observations obtained by rain gauge with simulations of 1-h rainfall from NoDA- and EnKF-initialized deterministic forecasts (with a 3-h lead time) valid at 1500, 1800, and 2100 UTC 23 July. At 1500 UTC 23 July, the first 3-h forecast initiated from the EnKF
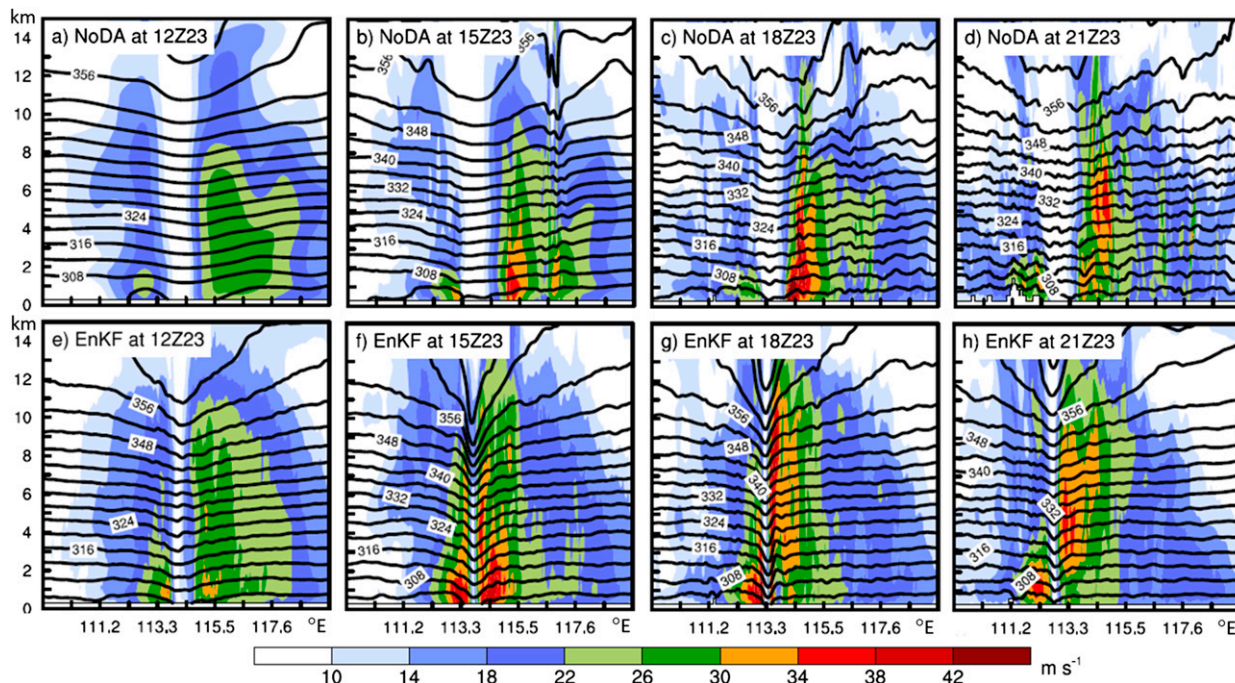
FIG. 9. East–west vertical cross sections of the analyzed horizontal wind speed (shaded, m s^{-1}) and potential temperature (contours, K) across the simulated TC center from (a)–(d) NoDA and (e)–(h) the EnKF analyses valid at 1200, 1500, 1800, and 2100 UTC 23 Jul 2012.

analyses at 1200 UTC produced improvement in both the pattern and magnitude of the 1-h rainfall relative to NoDA (Figs. 11a–c). NoDA had a larger areal coverage of precipitation than was observed but less rainfall near the TC center. Meanwhile the EnKF-initialized forecast successfully captured the intense precipitation

area near the TC center and the spiral rainbands in the Pearl River Delta region that includes Hong Kong and Guangzhou (though the areal coverage was still larger than the observed). To assess the improvement quantitatively, we calculated the 1-h rainfall threat scores (TS) for different thresholds (5, 10, 15, and 20 mm)
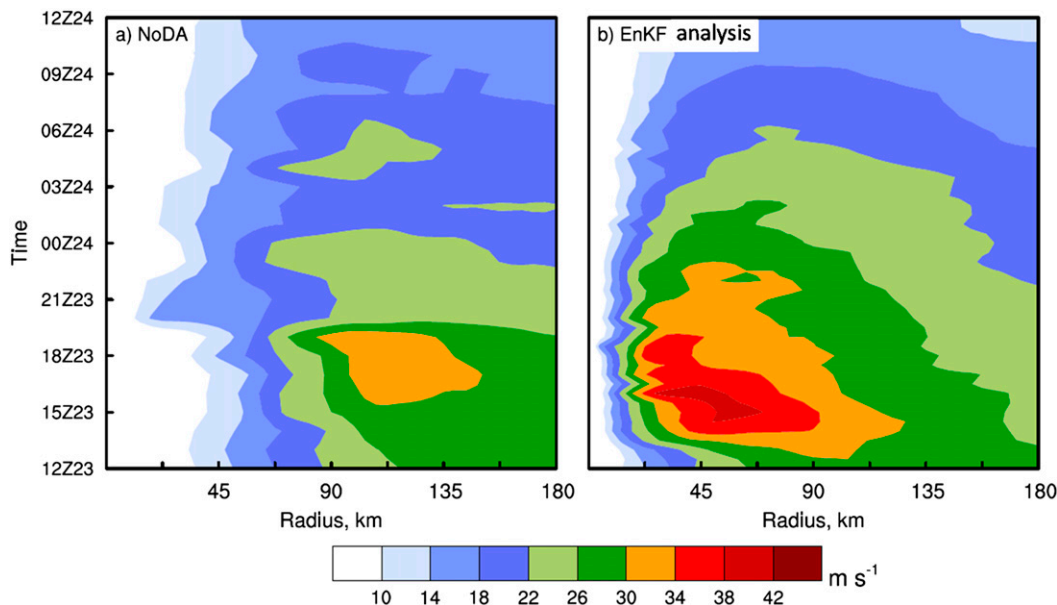
FIG. 10. Radius–time plots of the 850-hPa mean tangential winds (m s^{-1}) for (a) NoDA and (b) EnKF analysis.
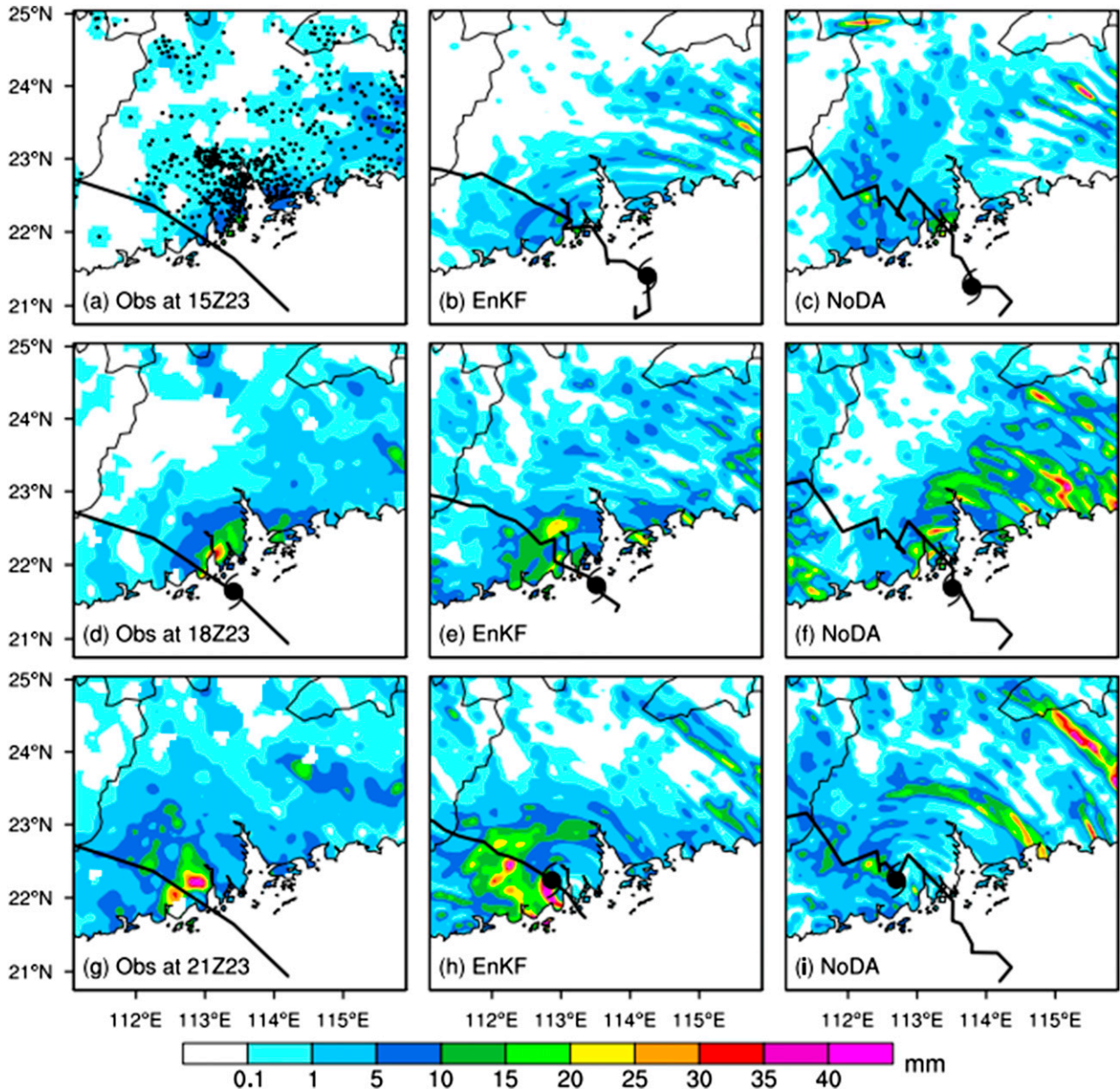
FIG. 11. (a),(d),(g) Observational analysis of the 1-h accumulated precipitation (mm) using automated weather station measurements (OBS); (b),(e),(h) the corresponding deterministic forecast initialized from the EnKF analysis with a 3-h lead time; and (c),(f),(i) the corresponding forecast from NoDA valid at (top) 1500, (middle) 1800, and (bottom) 2100 UTC 23 Jul 2012. The HKO best track, the TC track of the EnKF analysis ensemble mean, and the forecast TC track of NoDA as well as the corresponding TC position at the three times are also plotted for references.

over the plot area of Fig. 11. Results showed that the 1-h EnKF-initialized forecasts had higher TS than those of NoDA for all the thresholds except for 10 mm at this time (Fig. 12a).

The 1-h precipitation forecast from the EnKF analysis at 1800 UTC (Fig. 11e; a couple of hours before landfall) compared even more favorably (than NoDA) to the observed rainfall (Fig. 11d) in terms of both location and

minSLP (Fig. 11f), the latter of which overpredicted the rainfall in the eastern coastal areas of Guangdong Province. Consistently higher TS were observed in the EnKF prediction than that of NoDA for all the thresholds (Fig. 12b); the mean TS was about twice that of NoDA and much larger than that at 1500 UTC 23 July.

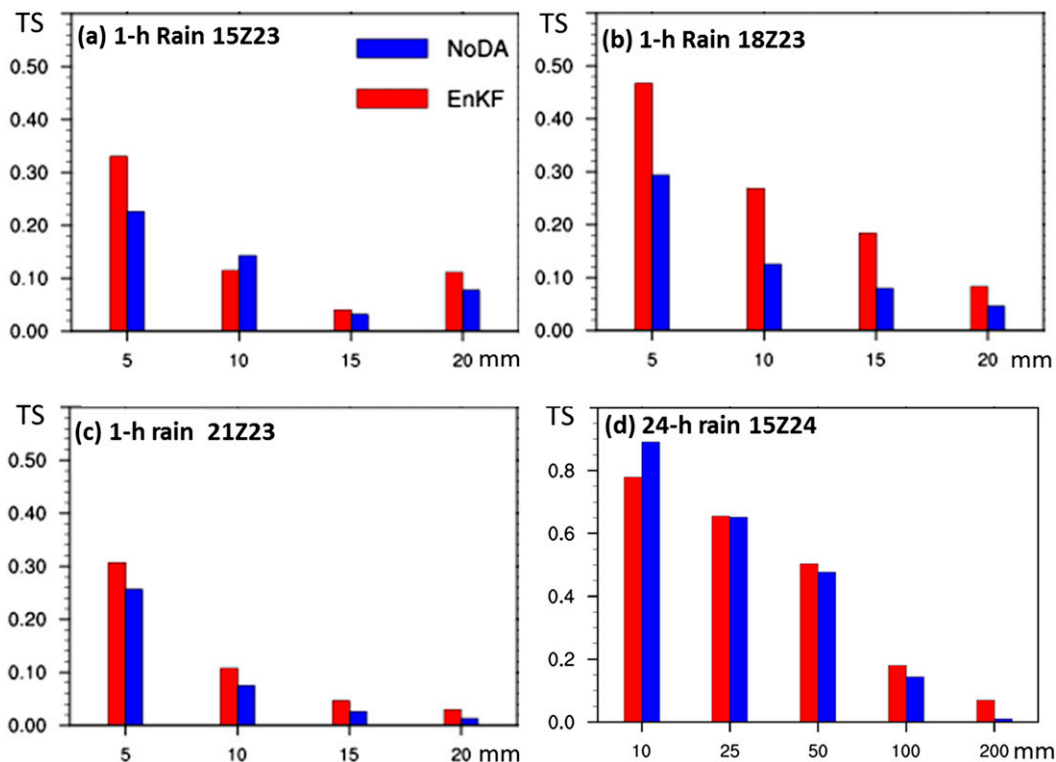The rainfall in both the observations and the EnKF-initialized forecasts was the most intense during

FIG. 12. Threat score of 1-h rainfall for different thresholds valid at (a) 1500, (b) 1800, and (c) 2100 UTC 23 Jul and (d) 24-h rainfall valid at 1500 UTC 24 Jul for NoDA and deterministic forecasts initialized from the EnKF analysis (a)–(c) 3 h and (d) 24 h before.

Vicente's landfall (1-h accumulation valid at 2100 UTC), though the EnKF-based prediction produced too much precipitation (Figs. 11g,h). The NoDA simulation nearly completely missed most of the intense rainfall near the observed landfall location just west of the Pearl River Delta region (Fig. 11i). Again, consistently higher TS were observed in the EnKF prediction than in NoDA though both EnKF and NoDA had lower TS (and a smaller improvement of EnKF over NoDA) at the landfalling stage than at other times (Fig. 12c). The largest relative improvement was obtained in the intense rainfall greater than 20 mm.

The simulated 24-h accumulated precipitation valid from 1500 UTC 23 July to 1500 UTC 24 July 2012 of the EnKF and NoDA were also compared with observations (Fig. 13). Consistent with the 1-h accumulation comparisons above, and despite some overestimation of the most intense rainfall by the EnKF-initialized forecasts, the overall 24-h accumulated rainfall forecast initialized with the EnKF assimilation of the Doppler radar observation was much better than the NoDA simulation throughout the region. Improvement was evident for intense rainfall greater than 50 mm, which

can be clearly seen in the comparison of 24-h rainfall TS (Fig. 12d).

5. Ensemble forecasts and sensitivity analyses

a. TC track and minSLP

In addition to deterministic forecasts initiated from the EnKF mean analyses, two 60-member ensemble forecasts were initialized from the ensemble analyses of the EnKF. One started at 1500 UTC, before the storm's landfall, and the other started at 2100 UTC, right after its landfall. Figures 14a and 14b show the simulated minSLP and tracks of Vicente from the two ensemble forecasts, along with the two deterministic forecasts from the mean EnKF analyses starting at the same times. The ensemble initialized from 1500 UTC showed larger uncertainty in the short-term forecast of the storm's minimum minSLP before Vicente's landfall than that after Vicente's landfall. The 3-h forecasts of minSLP (valid at 1800 UTC) from different ensemble members varied from 939 to 957 hPa, which covered well both best track estimates and the deterministic forecast from the EnKF mean analysis (Fig. 14a). However, the ensemble forecast of minSLP initialized
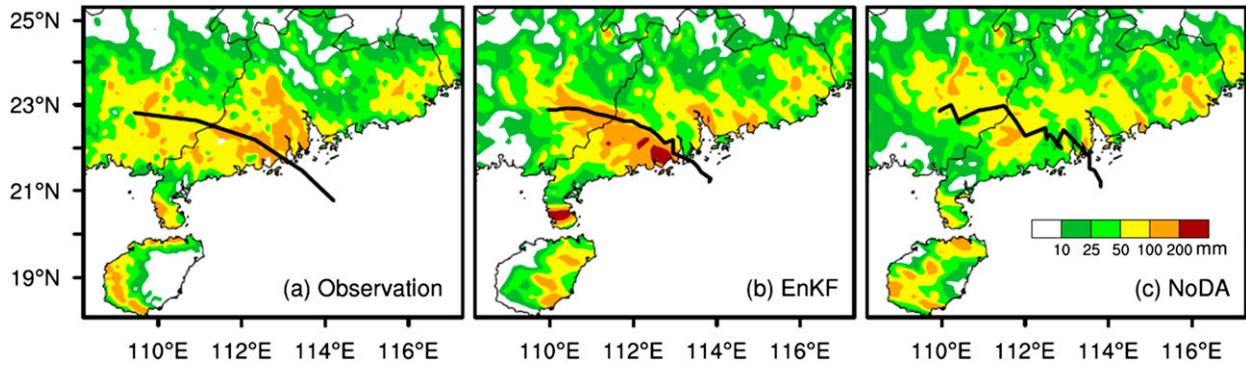
FIG. 13. The 24-h accumulated precipitation (mm) valid at 1500 UTC 24 Jul 2012 for (a) the observational analysis, (b) the deterministic forecast initialized from the EnKF analysis at 1500 UTC 23 Jul, and (c) NoDA. The corresponding TC tracks are also shown for references.

from 1500 UTC was systematically lower than the best track estimate after the storm's landfall (Fig. 14a), which was also noted in section 4 for the deterministic EnKF forecast.

The uncertainty in the track forecasts from the 1500 UTC ensemble was somewhat opposite of that of minSLP. All ensemble members were tightly clustered around the best track estimate at the initial and earlier
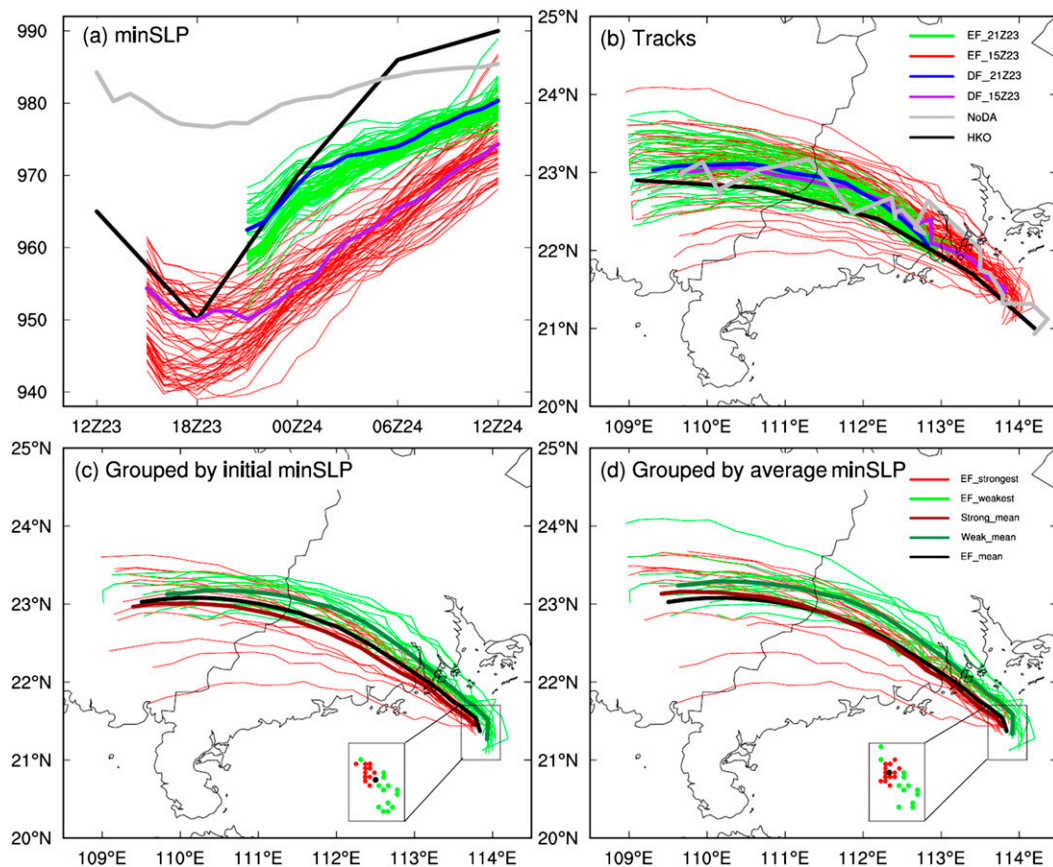

FIG. 14. Forecasts from two 60-member ensembles initialized from 1500 (red) and 2100 UTC (green) 23 Jul 2012 in comparison with the HKO best track estimate, the deterministic forecasts from the corresponding mean EnKF analyses, as well as NoDA for (a) minSLP and (b) tracks. The tracks of the ensemble initialized from 1500 UTC were grouped into the strongest (red) and weakest (green) 25% in terms of (c) initial and (d) average minSLP over 1500, 1800, and 2100 UTC 23 Jul and 0000, 0300, and 0600 UTC 24 Jul. Also plotted in (c),(d) are the initial TC positions of the two groups as well as the ensemble mean TC position (black dot).
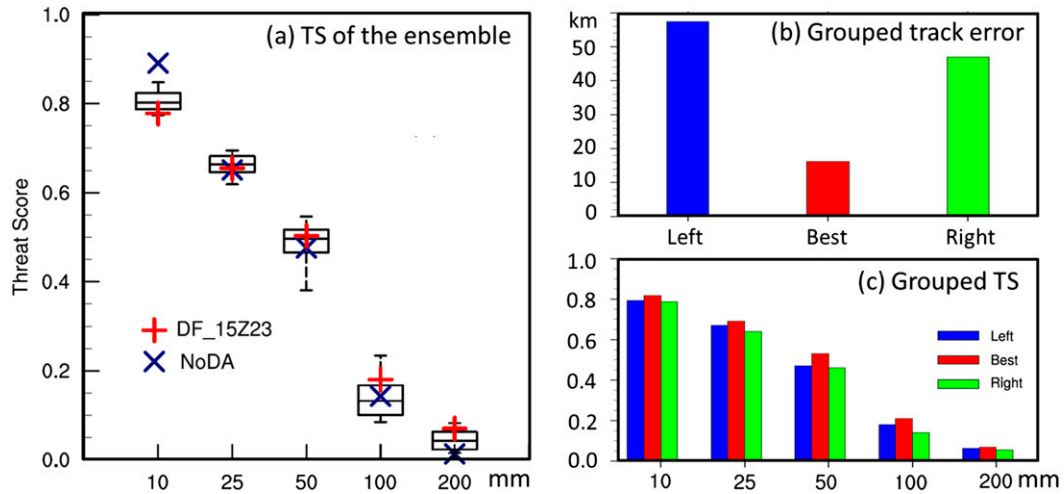
FIG. 15. (a) Box-and-whisker plot of the TS of the whole ensemble forecast initiated from the EnKF analysis ensemble at 1500 UTC 23 Jul for different rainfall thresholds. Also plotted are the TSs of the deterministic forecasts initiated from the EnKF mean analysis at 1500 UTC 23 Jul and NoDA. The shaded box covers the 25th–75th percentiles. The whiskers extend to the 10th and 90th percentiles, and the median value is marked by the horizontal line within each box. The mean (b) track error and (c) TS for the three groups according to their closeness to the best track are also plotted for references.

forecast times, though position spread increased during the decaying stage after the storm moved farther inland (Fig. 14b). The distance between different ensemble members was as large as 200–300 km in the 12–24-h forecasts, during which time the ensemble spread for the minSLP forecasts was greatly reduced due to the universal weakening of the storm after landfall (Fig. 14a).

Likely due to six more hours of radar data being assimilated, and also due to the weakening after the landfall, the uncertainty in the minSLP forecasts from the 2100 UTC ensemble (initialized right after landfall) was greatly reduced, compared to the 1500 UTC ensemble (Fig. 14a; green lines). The track uncertainty was also reduced, though there was still considerable spread after the decaying storm moved farther inland (Fig. 14b).

b. 24-h accumulated rainfall

Since the inland flooding was the leading cause of the loss of lives and property due to Vicente, it is natural to ask how uncertain the rainfall forecast was during and after the storm's landfall. The 24-h rainfall TS scores are shown in Fig. 15a for different thresholds of 10, 25, 50, 100, and 200 mm. The benefit of EnKF radar assimilation relative to NoDA was more apparent for more intense rainfall with the largest benefit obtained for 200-mm rainfall. The ensemble spread of the TS increased from the 10- to 100-mm thresholds and decreased again for the 200-mm threshold. For the 100-mm threshold, the 25 percentile was 0.1 while the 75 percentile was near 0.2. Another interesting result was that the TS of the deterministic forecast was below the 25 percentile for the 10-mm TS, closer to the medians of 25- and 50-mm TS, and higher than the 75 percentile of 100- and 200-mm rainfall TS.

The relationship between the 24-h rainfall distributions and TC tracks was then examined. Figure 16 shows the 24-h accumulated precipitation forecasts from 15 of the 60 ensemble members. These members were subjectively selected based on their track forecasts compared to HKO best track, which included five members with small averaged position error (left column), five with apparent deviations to the left side of the best track (middle column), and five members with apparent deviations to the right side of the best track (right column).

The rainfall patterns for different groups were very similar in terms of the juxtaposition of rainfall with the TC track. In general, the 24-h accumulated precipitation in each member was focused along the track, and members with the lowest track error had the best precipitation forecasts (Figs. 15b,c). The region with rainfall larger than 100 mm was mainly located immediately to the south of TC track for all the three groups (Fig. 16). As a result, TCs with a leftward track deviation had rainfall more to the south, while TCs with a rightward track deviation had rainfall more to the north. In addition, the more leftward the TC tracks deviated, the more extensive the rainfall larger than 100 mm was. This feature was even more clearly seen in the distribution of 200-mm accumulated rainfall. This result was also
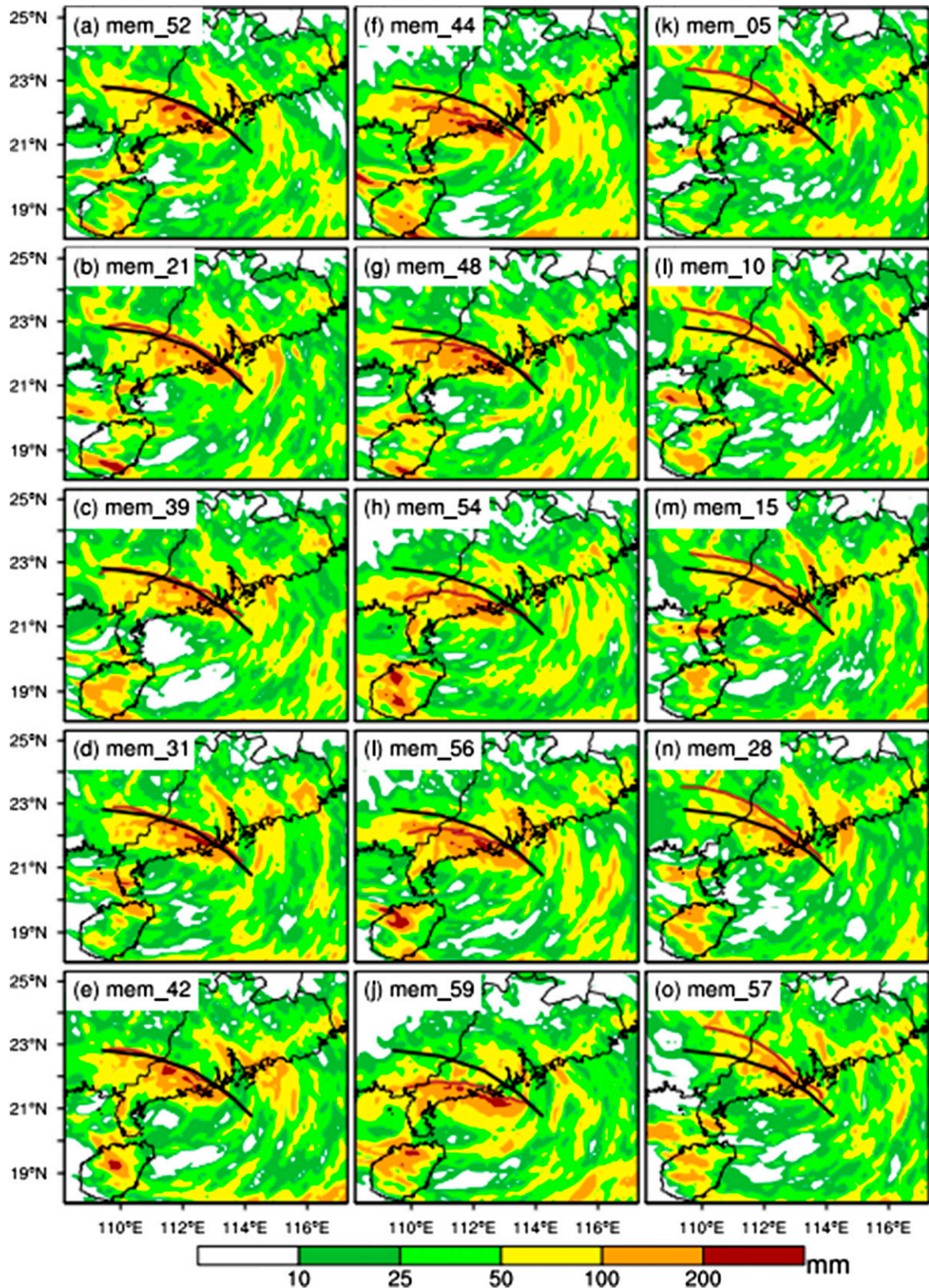
FIG. 16. As in Fig. 13, but for 15 selected ensemble members initialized at 1500 UTC 23 Jul 2012. The track of each ensemble is shown in each panel in brown in comparison with the ensemble mean track in black. (left) The five members with the simulated track close to the ensemble mean. The five members with the simulated track to the (middle) south and (right) north of the mean track.
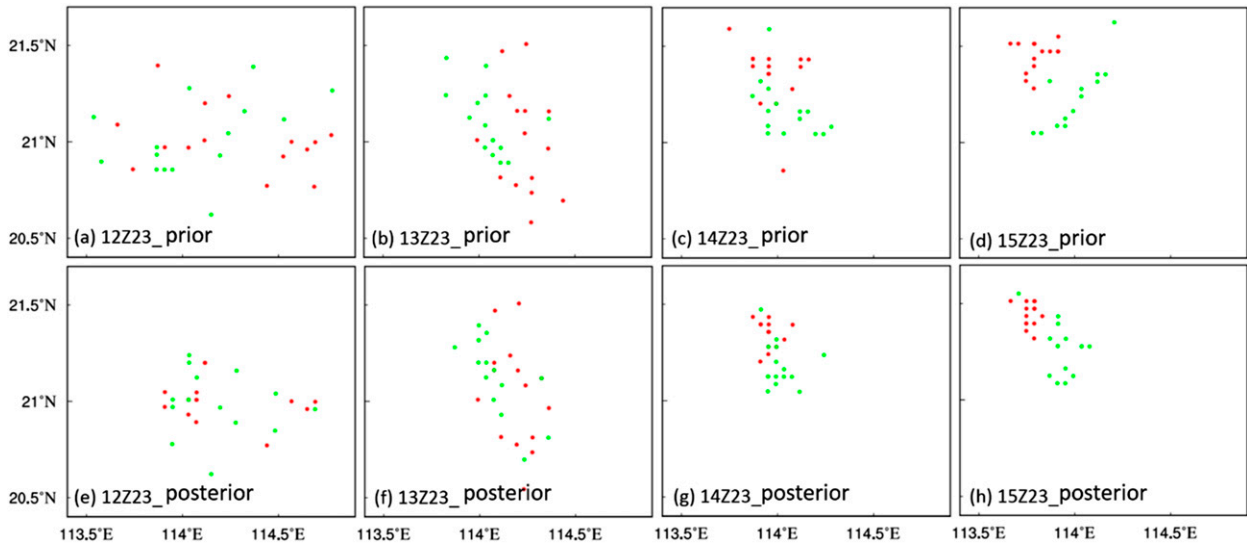
FIG. 17. The evolution of TC positions of the strongest 25% (red) and weakest 25% (green) members in both the (a)–(d) prior and (e)–(h) posterior ensemble from 1200 to 1500 UTC.

consistent with the higher TS for the leftward-biased tracks than those with a rightward bias. Large uncertainties were mainly observed in the location of rainfall larger than 100 mm among different groups. Even larger uncertainty was observed in the extent and location with rainfall larger than 200 mm among different groups or among different members in the same group. This suggests the most catastrophic and extreme forecasts to be associated with the largest uncertainties.

c. Ensemble sensitivity analysis

This subsection uses the ensemble sensitivity analysis to examine the controlling factors associated with the storm or the environment that might have led to the uncertainties revealed by the ensemble forecast initiated from the 1500 UTC analyses.

Results showed that the forecast uncertainties in TC track, minSLP, and precipitation were essentially a result of the initial relationship between TC minSLP and location. If ensemble forecast tracks are grouped by minSLP into the lowest (strongest) and highest (weakest) 25% (Fig. 14c), it is found that initially intense storms tended to be clustered near and to the northwest of the observed center, while initially weak storms were more spread out to the southeast. By examining the data assimilation cycling results, it was found that the initially random distribution of the weak and strong TC groups started to show this location bias in the 1-h forecast at 1400 UTC 23 July after two assimilation cycles (Fig. 17). This distribution became more apparent in the analysis ensemble at 1500 UTC.

The forecast tracks were closely related to this initial minSLP distribution. Figure 18 gives a schematic of the track features of the weak and strong groups as shown in Fig. 14c as well as the mean track of the strong and weak groups, the whole ensemble, and their initial positions. It shows that the initially strongest (weakest) ensemble members tended to have leftmost (rightmost) forecast tracks. The initially weaker storms at first moved cyclonically around the observed TC location and thus wound up mostly north of the mean track. Meanwhile, the initially stronger storms had fairly straight tracks to the south of the mean track. This track feature was mainly determined by the steering flow of the two groups. The steering flow was calculated by averaging the winds over a 300-km annulus from the TC center in the horizontal direction and 500–700 hPa in the vertical direction (Wu et al. 2007). Results showed that the weaker group had an initially more northward steering flow, resulting in the more northward track, which can be clearly seen from both group averages (Fig. 19a) and individual members (Fig. 19b). The stronger northward-steering flow at 1500 UTC is probably a result of the synoptic pattern (Fig. 19c) since the strong TC cases had higher heights to the north. Though the weaker storms were initially farther south, they moved northward quicker, which is demonstrated in the instantaneous correlation between TC latitude and minSLP (solid green in Fig. 20). In the meantime, the weaker storms were initially farther east, but later they were farther west, which can also be seen in the instant correlation between TC longitude and minSLP (dashed green in Fig. 20).

The impact of the initial minSLP distribution on the forecast track was first examined using the concept of
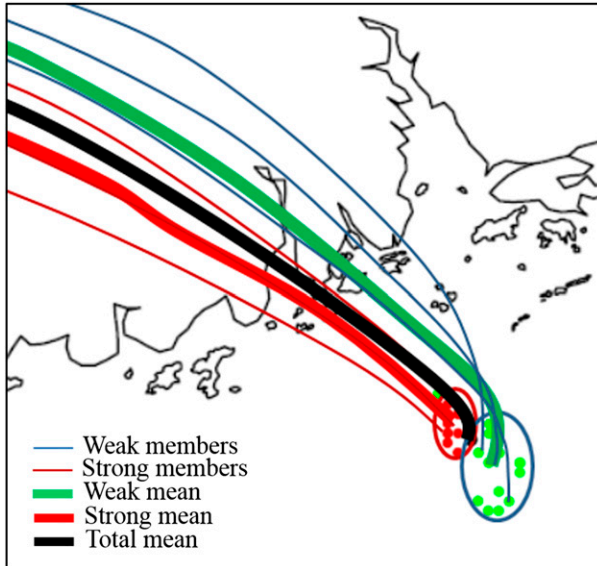
FIG. 18. A schematic of the track features of the weak and strong groups (thin lines), as well as the mean track of the strong and weak groups (heavy colored lines), the whole ensemble (heavy black line), and their initial positions (dots).

partial correlation. Assume we have independent variables x and z and a dependent variable y. To calculate partial correlation, first regress x on z and determine the residual e_{xz}, and then regress y on z to determine the residual e_{yz}. The correlation between e_{xz} and e_{yz} is the partial correlation between x and y with respect to z, which is denoted in this study by $r_{xy|z}$ [this is similar to Sippel et al. (2011)]. More concisely, it can be calculated in a single equation with

$$r_{xy|z} = \frac{r_{yx} - r_{yz}r_{xz}}{\sqrt{1 - r_{yz}^2}\sqrt{1 - r_{xz}^2}}. \tag{1}$$

In the partial correlation, the effect of z is removed from both x and y. Results showed that for a storm of a given

initial latitude, a weaker initial storm moved farther north with a decreasing tendency through 24 h (solid red in Fig. 20a). This was likely due to the initial relationship between initial minSLP and longitude and the subsequent track as shown in Fig. 18. For a storm of a given initial minSLP, when the storm was initially farther north it tended to stay farther north (solid blue in Fig. 20a). This is clear for both the strong and weak TC groups (Figs. 20c,e).

The impact of the initial minSLP distribution on the forecast minSLP was then examined. Results showed that for a storm of an initial given latitude, if it was initially strong, it stayed strong (solid red in Fig. 20b). This was essentially a reflection of strong time-lag minSLP correlation (dashed red in Fig. 20b). For a storm of an initial given minSLP, when it was initially farther south it would be stronger later on (solid blue in Fig. 20b), which was likely dominated by the weak group due to its larger initial position variance (Figs. 20d,f). This could be because systems farther south in the weak group spent more time over water.

The 24-h accumulated precipitation was found to be correlated well with the forecast latitude at three different forecast times (Figs. 21a–c). A leftward track had lower latitude throughout the forecast and vice versa. The negative correlations to the left of the mean track indicate that the more leftward tracks (lower latitude) were associated with stronger precipitation to the left of the mean track, while positive correlations indicate more rightward tracks (higher latitude) were associated with more precipitation along and to the right of the mean track. Interestingly, the dipole in correlation was not precisely over the ensemble mean track. The stripe of the positive correlation followed the ensemble mean track. This was likely because the heaviest precipitation was to the south of the center, thus any positive perturbation to latitude would result in heavy rainfall over the ensemble mean track location.
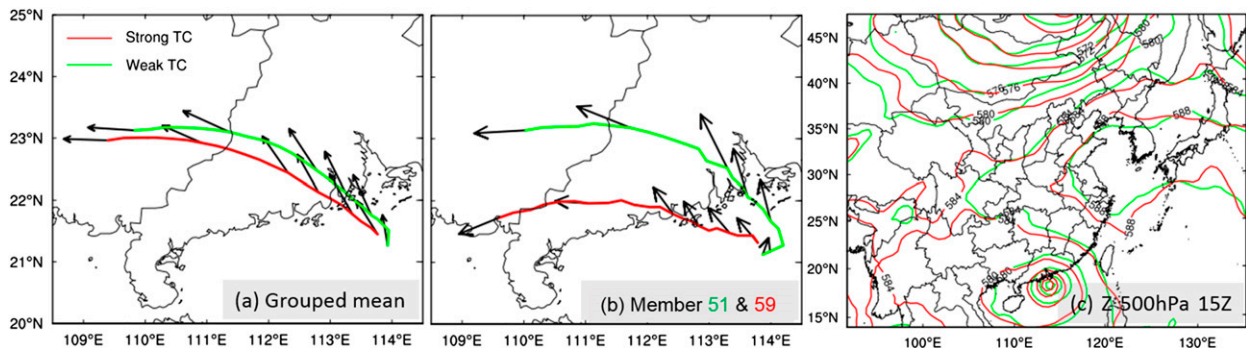

FIG. 19. The steering flow (black arrows) of (a) the weak (green) and strong (red) TC groups, and (b) two members from each group: member 51 (green) from the weak group and member 59 (red) from the strong group. (c) Also shown are the 500-hPa geopotential height (dam) of the strong member 59 (red) and the weak member 51 (green) at 1500 UTC 23 Jul.
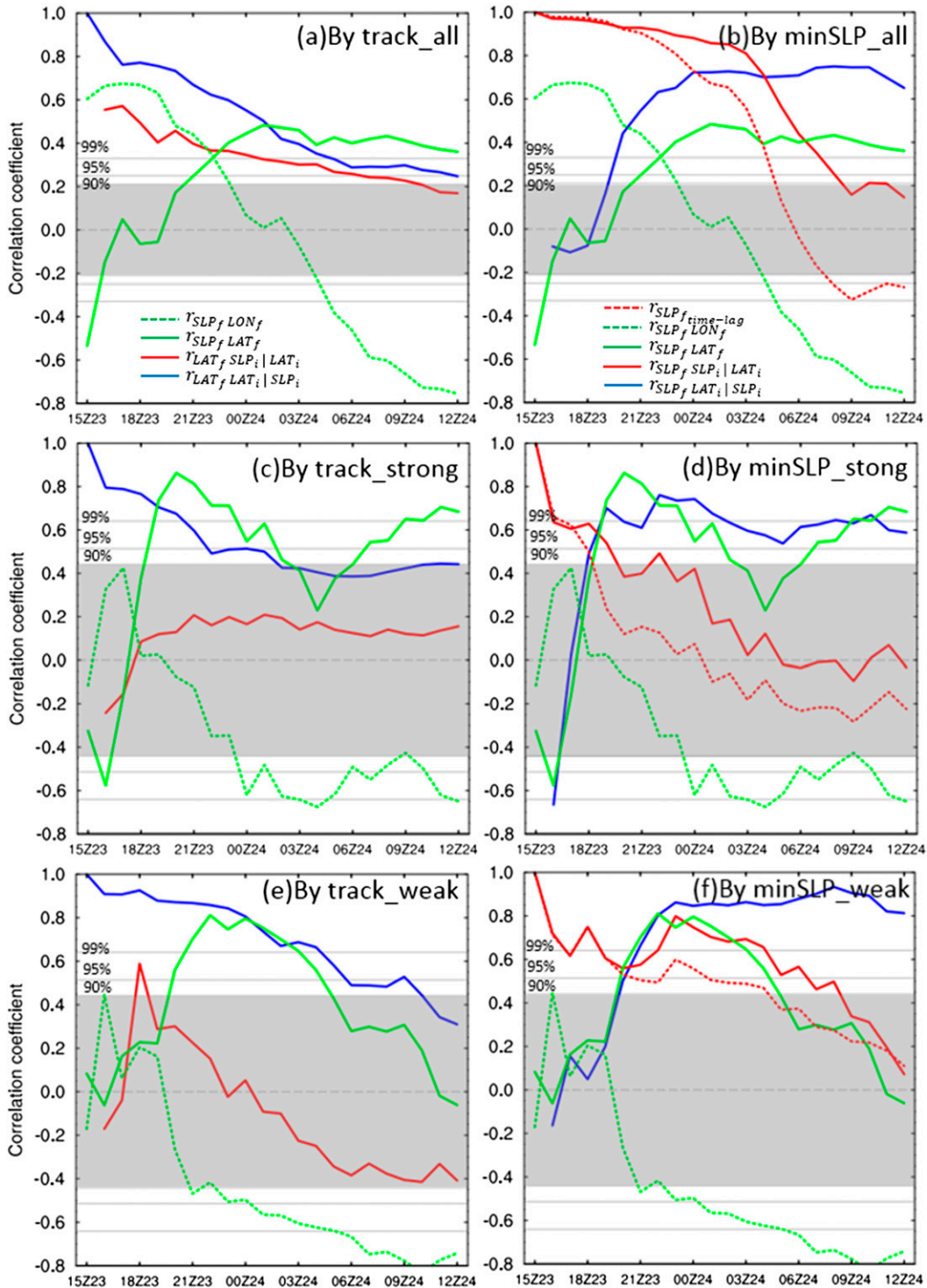
FIG. 20. The relationship between track and minSLP. Red and blue solid lines show partial correlation calculations with (a) track and (b) minSLP as the independent variable. The instantaneous correlation coefficient between the TC track and minSLP is plotted in green. The three gray lines denote the lower limit with 90%, 95%, and 99% confidence, respectively. The dashed red line in (b) denotes the time-lag correlation between initial and forecast minSLP. (c)–(f) As in (a),(b), for the strong and weak groups, respectively. The $r_{A_f A_i | B_i}$ denotes the partial correlation between variable A at forecast time f and variable A at initial time (1500 UTC 23 Jul, denoted by i) with respect to variable B at the initial time. The $r_{A_f B_f}$ denotes the instantaneous correlation coefficient between A and B at different forecast time f. The formula $r_{A_{f\_time-lag}}$ represents the time-lag correlation between initial and forecast A.
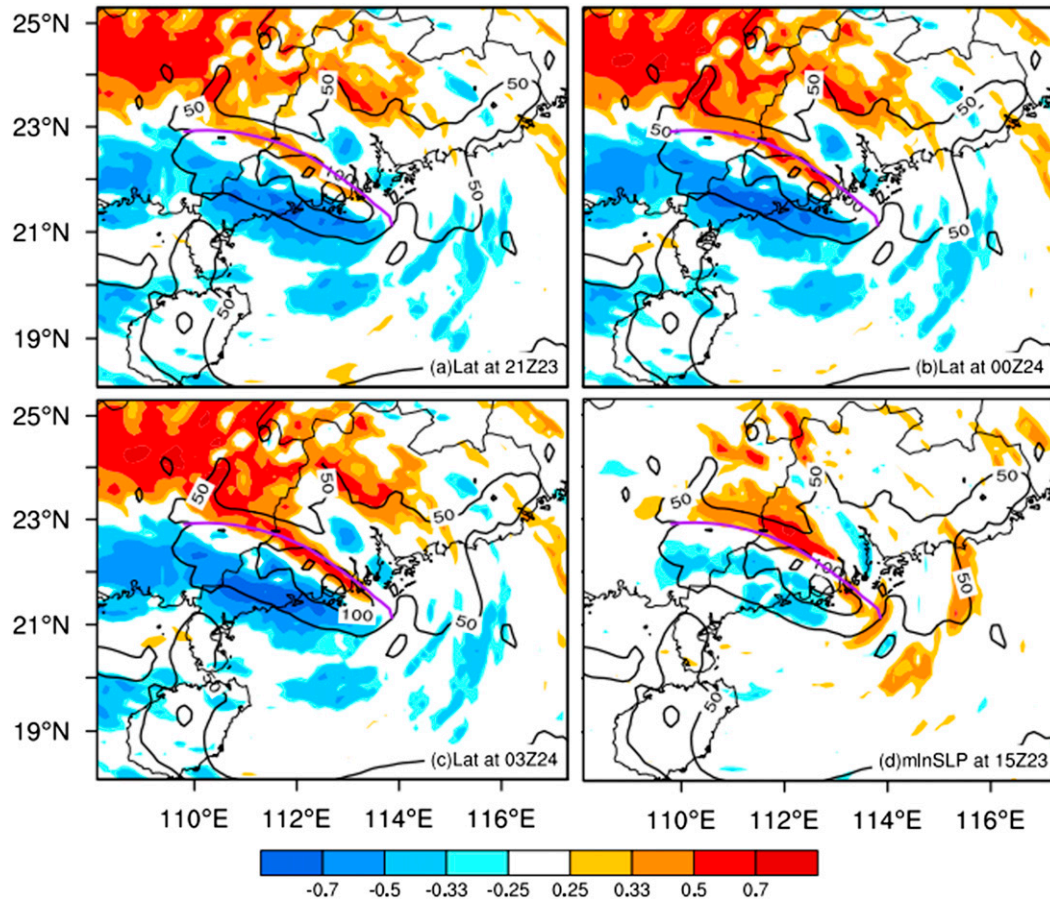
FIG. 21. Correlations (shaded) between the 24-h forecasted accumulated precipitation (mm) valid at 1500 UTC 24 Jul 2012 and the forecasted TC positions in terms of latitude at (a) 2100 UTC 23 Jul, (b) 0000 UTC 24 Jul, and (c) 0300 UTC 24 Jul 2012, and (d) the initial analysis of minSLP estimated from the 1500 UTC ensemble. The contours denote the ensemble-mean 24-h accumulated precipitation forecast (mm) and the purple line denotes the ensemble mean TC track.

Strong correlations (confidence level over 90%) were also observed between the 24-h accumulated precipitation and minSLP valid at 1500 UTC estimated for the 1500 UTC ensemble forecasts (Fig. 21d). It was evident that initially stronger storms tended to produce larger 24-h accumulated precipitation to the left of the ensemble mean track, while initially weaker storms tended to produce more precipitation to the right of the mean track. The correlation pattern between the 24-h rainfall and initial TC minSLP was quite similar to those between the 24-h rainfall and forecast TC positions (Figs. 21d vs 21a–c). This result was consistent with the significant correlation between the initial TC minSLP and forecast TC track, in which stronger TCs tended to move farther to the south.

6. Summary and conclusions

This work explored the performance of a WRF-based EnKF in continuous assimilation of Doppler radar data

in mainland China during the minimum minSLP stage of TC Vicente (2012). Vicente was an intense western North Pacific TC that made landfall in the Pearl River Delta region of Guangdong Province, China, around 2000 UTC 23 July 2012. The storm made landfall near minimum minSLP following rapid intensification, and it caused severe inland flooding.

Through the assimilation of radar radial velocity data at 30-min frequency, EnKF analyses successfully captured the track, the evolution of minSLP, and the inner-core structure of Vicente. The analyzed TC track followed well the best track estimates for both the timing and location of the landfall. After assimilating only 3–4 Doppler velocity volumes, the EnKF analysis was able to decrease the minSLP to the best track minSLP. Immediately after the first assimilation cycle, the inner structure of the TC significantly improved due to the asymmetric increments in wind and temperature fields. It was also found that the TC circulation improved both its outer and inner regions

during earlier assimilation cycles. Later on, most improvements were constrained to near or within the inner part of the TC circulation.

All the deterministic forecasts initiated from the ensemble mean of the EnKF analyses showed clear improvement in terms of TC track, minSLP, and precipitation compared with NoDA. The forecast landfall locations and times initialized from the EnKF mean analyses matched well with observations. With more data assimilated, the simulated tracks also became less noisy. Despite some timing error, forecasts near the minimum minSLP of the TC captured reasonably the observed minimum minSLP. However, these forecasts failed to weaken the TC as fast as in the observations. In addition, the 1-h precipitation forecast from the EnKF analysis compared more favorably to the observed rainfall in terms of both location and minSLP than did NoDA. The EnKF forecast successfully captured the intense precipitation area and the spiral rainbands in the Pearl River Delta region. Despite some overestimation of the most intense rainfall, the overall 24-h accumulated rainfall forecast initialized by the EnKF analyses was much improved over NoDA after only four volumes of the Doppler radial velocity being assimilated.

The ensemble forecasts initialized from the EnKF perturbations were further used to explore the dynamics and predictability of Vicente with respect to different lead times before and during the landfall. Larger uncertainty in the short-term forecast of the storm's minimum minSLP was observed before Vicente's landfall. Meanwhile, the uncertainty in the track forecasts increased with time. Furthermore, forecast uncertainties in the rainfall over land associated with TC Vicente was largely associated with track uncertainty. The intense rainfall (>50 mm) was tightly associated with the TC track mainly lying to the south of the TC track. Large uncertainty was observed in the extent and location along the track of the unusually catastrophic rainfall (>100 mm), which is a big challenge for disaster prevention.

Sensitivity analyses were further used to explore the leading dynamics that controlled the prediction and predictability of track, minSLP, and rainfall during and after TC landfall. Results showed that the initial relationship between TC minSLP, location, and the initial steering flow played an important role in the outcome of the subsequent forecast. In this case, the initially intense storms tended to be clustered near and to the northwest of the observed center, while initially weak storms were more spread out to the southeast. The weaker storms tended to have stronger initial southerly flow and ended up being farther north.

Results showed that the forecast track and minSLP were closely related to this initial minSLP distribution. The initially strongest (weakest) ensemble members tended to have a leftmost (rightmost) forecast track. Partial correlation analyses showed that a weaker initial storm at a given latitude moved farther north, and a storm of a given SLP that was initially farther north tended to stay farther north. Results also showed that an initially strong TC stayed strong. The initial latitude could be regarded as a factor impacting subsequent minSLP evolution considering that storms in the weak group appeared to intensify more or weaken less when they were initially farther south.

The 24-h accumulated precipitation was found to be correlated well with the forecast latitude. More leftward tracks (lower latitude) were associated with stronger precipitation to the left of the mean track, while more rightward tracks (higher latitude) were associated with more precipitation along and to the right of the mean track. Since stronger TCs tended to move farther south, a similar correlation was observed between the initial TC minSLP and TC 24-h accumulated precipitation.

Overall, results of this work clearly demonstrate the significance and potential of assimilating land-based Doppler radar observations with an EnKF in the initialization and prediction for TC Vicente. It provides a good example for the potential benefits of assimilating coastal radar data using ensemble-based data assimilation to improve operational TC forecasts. Note that the system described here may serve as a prototype for future forecasts and warnings, but that improvements, especially in the timeliness of the forecast output, must be made before such a system becomes feasible for operational use.

REFERENCES

Aberson, S. D., A. Aksoy, K. J. Sellwood, T. Vukicevic, and X. Zhang, 2015: Assimilation of high-resolution tropical cyclone observations with an ensemble Kalman filter using

HEDAS: Evaluation of 2008–11 HWRF forecasts. *Mon. Wea. Rev.*, **143**, 511–523, doi:10.1175/MWR-D-14-00138.1.

Aksoy, A., D. C. Dowell, and C. Snyder, 2009: A multicase comparative assessment of the ensemble Kalman filter for assimilation of radar observations. Part I: Storm-scale analyses. *Mon. Wea. Rev.*, **137**, 1805–1824, doi:10.1175/2008MWR2691.1.

——, ——, and ——, 2010: A multicase comparative assessment of the ensemble Kalman filter for assimilation of radar observations. Part II: Short-range ensemble forecasts. *Mon. Wea. Rev.*, **138**, 1273–1292, doi:10.1175/2009MWR3086.1.

——, S. Lorsolo, T. Vukicevic, K. J. Sellwood, S. D. Aberson, and F. Zhang, 2012: The HWRF Hurricane Ensemble Data Assimilation System (HEDAS) for high-resolution data: The impact of airborne Doppler radar observations in an OSSE. *Mon. Wea. Rev.*, **140**, 1843–1862, doi:10.1175/MWR-D-11-00212.1.

——, S. D. Aberson, T. Vukicevic, K. J. Sellwood, S. Lorsolo, and X. Zhang, 2013: Assimilation of high-resolution tropical cyclone observations with an ensemble Kalman filter using NOAA/AOML/HRD's HEDAS: Evaluation of the 2008–11 vortex-scale analyses. *Mon. Wea. Rev.*, **141**, 1842–1865, doi:10.1175/MWR-D-12-00194.1.

Barker, D., W. Huang, Y. Guo, A. Bourgeois, and Q. Xiao, 2004: A three-dimensional variational data assimilation system for MM5: Implementation and initial results. *Mon. Wea. Rev.*, **132**, 897–914, doi:10.1175/1520-0493(2004)132<0897:ATVDAS>2.0.CO;2.

Cangialosi, J. P., and J. L. Franklin, 2011: 2010 National Hurricane Center forecast verification report. NOAA/NHC, 77 pp. [Available online at http://www.nhc.noaa.gov/verification/pdfs/Verification_2010.pdf.]

Dong, J., and M. Xue, 2013: Assimilation of radial velocity and reflectivity data from coastal WSR-88D radars using ensemble Kalman filter for the analysis and forecast of landfalling Hurricane Ike (2008). *Quart. J. Roy. Meteor. Soc.*, **139**, 467–487, doi:10.1002/qj.1970.

Dowell, D. C., F. Zhang, L. J. Wicker, C. Snyder, and N. A. Crook, 2004: Wind and thermodynamic retrievals in the 17 May 1981 Arcadia, Oklahoma, supercell: Ensemble Kalman filter experiments. *Mon. Wea. Rev.*, **132**, 1982–2005, doi:10.1175/1520-0493(2004)132<1982:WATRIT>2.0.CO;2.

Du, N., M. Xue, K. Zhao, and J. Min, 2012: Impact of assimilating airborne Doppler radar velocity data using the ARPS 3DVAR on the analysis and prediction of Hurricane Ike (2008). *J. Geophys. Res.*, **117**, D18113, doi:10.1029/2012JD017687.

Evensen, G., 1994: Sequential data assimilation with a nonlinear quasi-geostrophic model using Monte Carlo methods to forecast error statistics. *J. Geophys. Res.*, **99**, 10 143–10 162, doi:10.1029/94JC00572.

Fovell, R. G., K. L. Corbosiero, A. Seifert, and K.-N. Liou, 2010: Impact of cloud-radiative processes on hurricane track. *Geophys. Res. Lett.*, **37**, L07808, doi:10.1029/2010GL042691.

Franklin, J. L., 2004: National Hurricane Center verification report. Preprints, *57th Interdepartmental Hurricane Conf.*, Miami, FL, Office of the Federal Coordinator for Meteorological Services and Supporting Research, 46 pp. [Available online at http://origin.www.nhc.noaa.gov/verification/pdfs/Verification_2004.pdf.]

Fujita, T., D. J. Stensrud, and D. C. Dowell, 2007: Surface data assimilation using an ensemble Kalman filter approach with initial condition and model physics uncertainties. *Mon. Wea. Rev.*, **135**, 1846–1868, doi:10.1175/MWR3391.1.

Gaspari, G., and S. E. Cohn, 1999: Construction of correlation functions in two and three dimensions. *Quart. J. Roy. Meteor. Soc.*, **125**, 723–757, doi:10.1002/qj.49712555417.

Grell, G. A., and D. Devenyi, 2002: A generalized approach to parameterizing convection combining ensemble and data assimilation techniques. *Geophys. Res. Lett.*, **29**, 1693, doi:10.1029/2002GL015311.

Hendricks, E. A., M. T. Montgomery, and C. A. Davis, 2004: The role of "vortical" hot towers in the formation of Tropical Cyclone Diana (1984). *J. Atmos. Sci.*, **61**, 1209–1232, doi:10.1175/1520-0469(2004)061<1209:TROVHT>2.0.CO;2.

Hong, S., J. Dudhia, and S. Chen, 2004: A revised approach to ice microphysical processes for the bulk parameterization of clouds and precipitation. *Mon. Wea. Rev.*, **132**, 103–120, doi:10.1175/1520-0493(2004)132<0103:ARATIM>2.0.CO;2.

Houze, R. A., S. S. Chen, B. F. Smull, W.-C. Lee, and M. M. Bell, 2007: Hurricane intensity and eyewall replacement. *Science*, **315**, 1235–1238, doi:10.1126/science.1135650.

Landsea, C. W., and J. L. Franklin, 2013: Atlantic Hurricane database uncertainty and presentation of a new database format. *Mon. Wea. Rev.*, **141**, 3576–3592, doi:10.1175/MWR-D-12-00254.1.

Li, Y., X. Wang, and M. Xue, 2012: Assimilation of radar radial velocity data with the WRF ensemble-3DVAR hybrid system for the prediction of Hurricane Ike (2008). *Mon. Wea. Rev.*, **140**, 3507–3524, doi:10.1175/MWR-D-12-00043.1.

Liu, Z., C. S. Schwartz, C. Snyder, and S. Y. Ha, 2012: Impact of assimilating AMSU-A radiances on forecasts of 2008 Atlantic tropical cyclones initialized with a limited-area ensemble Kalman filter. *Mon. Wea. Rev.*, **140**, 4017–4034, doi:10.1175/MWR-D-12-00083.1.

Meng, Z., and F. Zhang, 2007: Test of an ensemble Kalman filter for mesoscale and regional-scale data assimilation. Part II: Imperfect-model experiments. *Mon. Wea. Rev.*, **135**, 1403–1423, doi:10.1175/MWR3352.1.

——, and ——, 2008a: Test of an ensemble Kalman filter for mesoscale and regional-scale data assimilation. Part III: Comparison with 3DVAR in a real-data case study. *Mon. Wea. Rev.*, **136**, 522–540, doi:10.1175/2007MWR2106.1.

——, and ——, 2008b: Test of an ensemble Kalman filter for mesoscale and regional-scale data assimilation. Part IV: Performance over a warm-season month of June 2003. *Mon. Wea. Rev.*, **136**, 3671–3682, doi:10.1175/2008MWR2270.1.

Montgomery, M. T., M. E. Nicholls, T. A. Cram, and A. Saunders, 2006: A vortical hot tower route to tropical cyclogenesis. *J. Atmos. Sci.*, **63**, 355–386, doi:10.1175/JAS3604.1.

NOAA/National Centers for Environmental Prediction, 2000: NCEP FNL Operational Model Global Tropospheric Analyses, continuing from July 1999 (updated daily). National Center for Atmospheric Research Computational and Information Systems Laboratory Research Data Archive, doi:10.5065/D6M043C6.

Noh, Y., W.-G. Cheon, S.-Y. Hong, and S. Raasch, 2003: Improvement of the K-profile model for the planetary boundary layer based on large eddy simulation data. *Bound.-Layer Meteor.*, **107**, 401–427, doi:10.1023/A:1022146015946.

Oye, R., C. Mueller, and C. Smith, 1995: Software for radar data translation, visualization, editing and interpolation. Preprints, *27th Conf. on Radar Meteorology*, Vail, CO, Amer. Meteor. Soc., 359–361.

Rappaport, E. N., and Coauthors, 2009: Advances and challenges at the National Hurricane Center. *Wea. Forecasting*, **24**, 395–419, doi:10.1175/2008WAF2222128.1.

Rogers, R., and Coauthors, 2006: The Intensity Forecasting Experiment: A NOAA multiyear field program for improving tropical cyclone intensity forecasts. *Bull. Amer. Meteor. Soc.*, **87**, 1523–1537, doi:10.1175/BAMS-87-11-1523.

Shieh, O. H., M. Fiorino, M. E. Kucas, and B. Wang, 2013: Extreme rapid intensification of Typhoon Vicente (2012) in the South China Sea. *Wea. Forecasting*, **28**, 1578–1587, doi:10.1175/WAF-D-13-00076.1.

Sippel, J. A., S. A. Braun, and C. Shie, 2011: Environmental influences on the strength of Tropical Storm Debby (2006). *J. Atmos. Sci.*, **68**, 2557–2581, doi:10.1175/2011JAS3648.1.

——, S. Braun, F. Zhang, and Y. Weng, 2013: Ensemble Kalman filter assimilation of simulated HIWRAP Doppler velocity data in a hurricane. *Mon. Wea. Rev.*, **141**, 2683–2704, doi:10.1175/MWR-D-12-00157.1.

——, F. Zhang, Y. Weng, L. Tian, G. M. Heymsfield, and S. A. Braun, 2014: Ensemble Kalman filter assimilation of HIWRAP observations of Hurricane Karl (2010) from the unmanned Global Hawk aircraft. *Mon. Wea. Rev.*, **142**, 4559–4580, doi:10.1175/MWR-D-14-00042.1.

Skamarock, W. C., and Coauthors, 2008: A description of the Advanced Research WRF version 3. NCAR Tech. Note NCAR/TN-475+STR, 113 pp. [Available online at http://www.mmm.ucar.edu/wrf/users/docs/arw_v3_bw.pdf.]

Snyder, C., and F. Zhang, 2003: Tests of an ensemble Kalman filter for convective-scale data assimilation. *Mon. Wea. Rev.*, **131**, 1663–1677, doi:10.1175//2555.1.

Tong, M., and M. Xue, 2005: Ensemble Kalman filter assimilation of Doppler radar data with a compressible nonhydrostatic model: OSS experiments. *Mon. Wea. Rev.*, **133**, 1789–1807, doi:10.1175/MWR2898.1.

Wang, B., and X. Zhou, 2008: Climate variation and prediction of rapid intensification in tropical cyclones in the western North Pacific. *Meteor. Atmos. Phys.*, **99**, 1–16, doi:10.1007/s00703-006-0238-z.

Wang, M., M. Xue, K. Zhao, and J. Dong, 2014: Assimilation of T-TREC-retrieved winds from single-Doppler radar with an ensemble Kalman filter for the forecast of Typhoon Jangmi (2008). *Mon. Wea. Rev.*, **142**, 1892–1907, doi:10.1175/MWR-D-13-00387.1.

Wang, Y., 2002: Vortex Rossby waves in a numerically simulated tropical cyclone. Part I: Overall structure, potential vorticity, and kinetic energy budgets. *J. Atmos. Sci.*, **59**, 1213–1238, doi:10.1175/1520-0469(2002)059<1213:VRWIAN>2.0.CO;2.

Weng, Y., and F. Zhang, 2012: Assimilating airborne Doppler radar observations with an ensemble Kalman filter for convection-permitting hurricane initialization and prediction: Katrina (2005). *Mon. Wea. Rev.*, **140**, 841–859, doi:10.1175/2011MWR3602.1.

Wu, C.-C., J.-H. Chen, P.-H. Lin, and K.-H. Chou, 2007: Targeted observations of tropical cyclone movement based on the adjoint-derived sensitivity steering vector. *J. Atmos. Sci.*, **64**, 2611–2626, doi:10.1175/JAS3974.1.

——, G.-Y. Lien, J.-H. Chen, and F. Zhang, 2010: Assimilation of tropical cyclone track and structure based on the ensemble Kalman filter (EnKF). *J. Atmos. Sci.*, **67**, 3806–3822, doi:10.1175/2010JAS3444.1.

Xiao, Q., Y. H. Kuo, J. Sun, W. C. Lee, D. M. Barker, and E. Lim, 2007: An approach of radar reflectivity data assimilation and its assessment with the inland QPF of Typhoon Rusa (2002) at landfall. *J. Appl. Meteor. Climatol.*, **46**, 14–22, doi:10.1175/JAM2439.1.

Xu, D., Z. Liu, X.-Y. Huang, J. Min, and H. Wang, 2013: Impact of assimilating IASI radiance observations on forecasts of two tropical cyclones. *Meteor. Atmos. Phys.*, **122**, 1–18, doi:10.1007/s00703-013-0276-2.

Xue, M., and J. Dong, 2013: Impact of assimilating best track minimum sea level pressure data together with coastal Doppler radar data on hurricane analysis and prediction at a cloud-resolving resolution. *Acta Meteor. Sin.*, **27**, 379–399, doi:10.1007/s13351-013-0304-7.

Zhang, F., and Y. Weng, 2015: Predicting hurricane intensity and associated hazards: A five-year real-time forecast experiment with assimilation of airborne Doppler radar observations. *Bull. Amer. Meteor. Soc.*, **96**, 25–33, doi:10.1175/BAMS-D-13-00231.1.

——, C. Snyder, and J. Sun, 2004: Tests of an ensemble Kalman filter for convective-scale data assimilation: Impact of initial estimate and observations. *Mon. Wea. Rev.*, **132**, 1238–1253, doi:10.1175/1520-0493(2004)132<1238:IOIEAO>2.0.CO;2.

——, Z. Meng, and A. Aksoy, 2006: Test of an ensemble Kalman filter for mesoscale and regional-scale data assimilation. Part I: Perfect model experiments. *Mon. Wea. Rev.*, **134**, 722–736, doi:10.1175/MWR3101.1.

——, Y. Weng, J. A. Sippel, Z. Meng, and C. H. Bishop, 2009: Cloud resolving hurricane initialization and prediction through assimilation of Doppler radar observations with an ensemble Kalman filter. *Mon. Wea. Rev.*, **137**, 2105–2125, doi:10.1175/2009MWR2645.1.

——, ——, J. F. Gamache, and F. D. Marks, 2011: Performance of convection-permitting hurricane initialization and prediction during 2008–2010 with ensemble data assimilation of inner-core airborne Doppler radar observations. *Geophys. Res. Lett.*, **38**, L15810, doi:10.1029/2011GL048469.

Zhu, X., and J. Zhu, 2004: New generation weather radar network in China. *Meteor. Sci. Technol.*, **32** (4), 255–258.

Zou, X., and Q. Xiao, 2000: Studies on the initialization and simulation of a mature hurricane using a variational bogus data assimilation scheme. *J. Atmos. Sci.*, **57**, 836–860, doi:10.1175/1520-0469(2000)057<0836:SOTIAS>2.0.CO;2.